Princeton Plasma Physics Laboratory

PPPL- 4278

PPPL- 4278

The Theory of Variances in Equilibrium Reconstruction

Leonid E. Zakharov, Jerome Lewandowski,
Elizabeth L. Foley, Fred M. Levinton, Howard Y. Yuh,
Vladimir Drozdov, and Darren McDonald

January 2008

Prepared for the U.S. Department of Energy under Contract DE-AC02-76CH03073.

Princeton Plasma Physics Laboratory
Report Disclaimers

Full Legal Disclaimer

Trademark Disclaimer

PPPL Report Availability

Princeton Plasma Physics Laboratory:

http://www.pppl.gov/techreports.cfm

Office of Scientific and Technical Information (OSTI):

http://www.osti.gov/bridge

Related Links:

U.S. Department of Energy

Office of Scientific and Technical Information

Fusion Links

The theory of variances in equilibrium reconstruction

Leonid E. Zakharov[1], Jerome Lewandowski[1],
Elizabeth L. Foley[2], Fred M. Levinton[2], Howard Y. Yuh[2]
Vladimir Drozdov[3], Darren McDonald[3]

[1] *PPPL, Princeton University, Princeton NJ, 08543 USA*
[2] *Nova Photonics, Princeton NJ, 08540 USA*
[3] *JET, EFDA, Culham UK*

July 17, 2007

For easy navigation the enumeration in the Table of Contents, and the "(to ToC)" right after the section names are the forward and backward hyperlinks between Table of Contents and the beginning of sections.

Contents

Abstract

The theory of variances of equilibrium reconstruction is presented. It complements existing practices with information regarding what kind of plasma profiles can be reconstructed, how accurately, and what remains beyond the abilities of diagnostic systems. The σ-curves, introduced by the present theory, give a quantitative assessment of quality of effectiveness of diagnostic systems in constraining equilibrium reconstructions. The theory also suggests a method for aligning the accuracy of measurements of different physical nature.

1 Introduction *(to ToC)*

The solution of the Grad-Shafranov (GSh) equation [1]

$$\Delta^*\bar{\Psi} \equiv \frac{\partial^2\bar{\Psi}}{\partial r^2} - \frac{1}{r}\frac{\partial\bar{\Psi}}{\partial r} + \frac{\partial^2\bar{\Psi}}{\partial z^2} = -T - r^2P, \quad \bar{\Psi} \equiv \frac{\Psi}{2\pi}, \quad T = T(\bar{\Psi}) \equiv \bar{F}\frac{d\bar{F}}{d\bar{\Psi}}, \quad P = P(\bar{\Psi}) \equiv \frac{d\bar{p}}{d\bar{\Psi}},$$
$$\mathbf{B} = \mathbf{B}_{pol} + \frac{1}{r}\bar{F}(\bar{\Psi})\mathbf{e}_\varphi, \quad \mathbf{B}_{pol} = \frac{1}{r}(\nabla\bar{\Psi}\times\mathbf{e}_\varphi), \quad \bar{p} = \mu_0 p(\bar{\Psi}), \quad \bar{j} \equiv \mu_0 j_\varphi = \frac{1}{r}T + rP \tag{1.1}$$

gives the most basic information on the magnetic configuration, which is necessary for all physics models of the tokamak plasma. Here, r, φ, z, are cylindrical coordinates reflecting axisymmetry of tokamak plasma, Ψ is the poloidal magnetic flux, B_φ is the toroidal magnetic field, p is the plasma pressure, and j_φ is the toroidal current density.

The equation (1.1) is two-dimensional, and its solution $\bar{\Psi}(r,z)$ is determined by the shape of the plasma boundary and by the two one-dimensional functions $T(\bar{\Psi}), P(\bar{\Psi})$ in the right hand side representing the current distribution inside the plasma. Correspondingly, the variances in the magnetic configurations are related to uncertainties in the plasma boundary and in two profiles $T(\bar{\Psi}), P(\bar{\Psi})$. The present paper gives the theory, which allows the evaluation of these variances in equilibrium reconstruction.

Determination of the plasma boundary from external magnetic measurements can be considered as a separate problem, not directly related to the GSh equation. Its reconstruction is linked in a straightforward way with the accuracy of external magnetic measurements, which can be improved upon necessity. We have intentionally neglected (except for one example) the discussion of boundary reconstruction in orderto focus on the more challenging problem of reconstruction of plasma profiles.

If the plasma boundary is reconstructed in some manner, the measured distribution of the magnetic field $\mathbf{B}_{pol}$ along the plasma boundary restricts the choice of the two functions P, T in the right hand side of the GSh equation. This effect, evident in equilibrium calculations of non-circular plasmas, motivated the first equilibrium reconstruction as early as the 1970s [2] in an attempt to recover the current density (and magnetic configuration) from information on the measured $\mathbf{B}_{pol}$ outside the plasma. At present, reconstruction is a standard tool for interpreting the geometry of magnetic configurations due to the wide use of the EFIT code [3, 4] and its modifications.

Nevertheless, having only external measurements in tokamaks, the two unknown functions in the right hand side of Eq.(1.1) can be reconstructed only in a limited way. Thus, in tokamaks with a circular cross-section (in a high aspect ratio approximation) only integral parameters such as plasma current I_{pl}, internal inductance l_i and Shafranov's β_j [5] can be determined from external magnetic measurements (which include the diamagnetic loop). An outstanding example of a non-circular configuration with the same property of "hiddenness" was theoretically described by Bishop and Taylor in 1985 [6, 7]. On the other hand, all equilibrium calculations show a distinctive effect of the current distribution on the external magnetic fields in non-circular plasmas, indicating that the shaping helps to retrieve more information about internal plasma profiles from external measurements.

But in any case, internal measurements are necessary. Because of the extreme importance of the equilibrium information, different diagnostics are being developed to provide additional information for reconstruction of the current distribution inside the plasma. Examples include kinetic measurements of electron and ion temperatures, plasma density, contribution of the fast particles into the plasma pressure, polarimetry (measuring the line integrated Faraday rotation of polarized light from the laser beam [8, 9], or spectral lines [10, 11, 12]), signals related to Motion Stark Effect (MSE) [13], position of resonant surfaces from internal magneto-hydrodynamic modes, etc.

Still, up to now, even with additional internal measurements the objective assessment of the value of equilibrium reconstruction has not been possible and the reconstruction itself remains a sort of "art" in numerical simulations rather than a science.

Here, we describe a rigorous method, based on analysis of linear perturbations of equilibria, which allows assessment of uncertainties in equilibrium reconstruction, its overall value, and the contribution of

measurements of different physical nature to the reconstruction. The same approach makes possible the quantitative evaluation of quality of the diagnostic systems on existing and future machines. For practical use, the theory was implemented into ESC (Equilibrium and Stability Code) [14], which is intrinsically based on linearization of the GSh equation as a method of its solution.

Sect. 2 describes reduction of the problem of variances in equilibrium reconstruction to a matrix problem, which can be solved using the SVD (Singular Value Decomposition) technique [16]. Sect. 3 introduces the variances in equilibrium reconstruction and σ-curves. Sect. 4 gives σ-curves for characteristic equilibrium configurations. Sect. 5 demonstrates the crucial role of internal measurements for reconstruction using the line polarization (MSE-LP) and line shift (MSE-LS) signals from the motional Stark effect as an example, relevant to the ITER diagnostics. Sect. 6 outlines the possibility of aligning the accuracy levels of different measurements. Sect. 7 addresses the issue of solving the non-linear, ill-posed problem of reconstruction for the GSh equation. It gives a rigorous practical recipe, based on σ-curves, for how to perform the actual reconstruction in a stable and accurate manner.

The Summary outlines the possible applications of the theory of variances and its extension to other types of reconstructions of either one- or two-dimensional sources of signals.

2 The formulation of the problem of variances *(to ToC)*

The theory of variances assumes that the reconstruction has been already performed and has generated a plasma shape and reconstructed functions $T(\bar\Psi), P(\bar\Psi)$. The question to answer is what kind of other equilibria are possible within the given accuracy of diagnostics.

This problem is reduced to solving the linearized equilibrium problem

$$\bar\Psi = \bar\Psi_0(a) + \psi, \quad \Delta^*\psi + T'_{\bar\Psi}\psi + P'_{\bar\Psi}\psi = -\delta T(a) - \delta P(a) r^2 \tag{2.1}$$

for N possible perturbations of the plasma boundary ξ,and the functions T and P, $\delta T, \delta P$, which can be represented as

$$\begin{gathered}
\xi = \sum_{n=0}^{n<N_\xi} A_n \xi^n(\theta), \quad \delta T = \sum_{n=0}^{n<N_J} T_n f^n(a), \quad \delta P = \sum_{n=0}^{n<N_P} P_n f^n(a), \\
N = N_\xi + N_J + N_P, \quad \xi^n = \begin{cases} \cos m\theta, & n = 2m, \quad m = 0, 1, \ldots, \\ \sin m\theta, & n = 2m-1, \quad m = 1, 2, \ldots, \end{cases}, \quad f^n = \cos\frac{\pi n a}{2},
\end{gathered} \tag{2.2}$$

where $0 \le a \le 1$ is the square root of the normalized toroidal flux, used throughout this paper as a flux coordinate, and θ is the poloidal angle on magnetic surface. The trigonometric basis functions $f^m(a)$ are used here as a particular choice.

Instead of functions $T(\bar\Psi), P(\bar\Psi)$ and their perturbations $\delta T(\bar\Psi), \delta P(\bar\Psi)$, most of results in this paper are presented using an equivalent pair of current densities $\bar\jmath_s(a), \bar\jmath_p(a)$ and their perturbations

$$\bar\jmath(a,r) = \frac{R_0}{r}\bar\jmath_s(a) + \left(\frac{r}{R_0} - \frac{R_0}{r}\right)\bar\jmath_p(a), \quad \bar\jmath_p(a) \equiv R_0 P, \quad \bar\jmath_s(a) \equiv \frac{T}{R_0} + R_0 P, \tag{2.3}$$

where R_0 is the radius of magnetic axis. Fig. 1 shows an example of the background current density profiles $\bar\jmath_s(a), \bar\jmath_p(a)$ and the basis functions $f^n(a)$.

The displacement ξ, used here, specifies the plasma boundary perturbation $\delta r(\theta), \delta z(\theta)$ in the following form

$$r(a+\xi,\theta) = r(a,\theta) + r'_a\xi, \quad z(a+\xi,\theta) = z(a,\theta) + z'_a\xi, \quad \delta r(\theta) = r'_a(\theta)\xi|_{a=1}, \quad \delta z(\theta) = z'_a(\theta)\xi|_{a=1}. \tag{2.4}$$

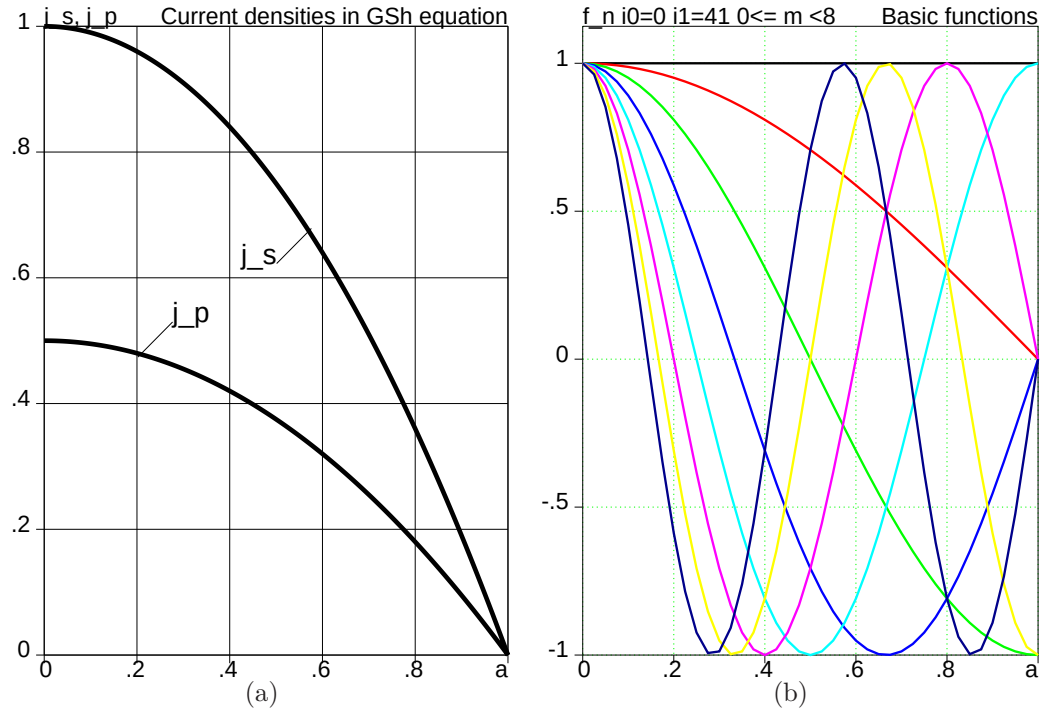

Figure 1: (a) Background current density profiles $\bar{j}_s(a), \bar{j}_p(a)$, and (b) trigonometric expansion functions $f^n(a)$

The displacement defined in this way is related to the solution of the linearized GSh equation (2.1)

$$\xi = -\left.\frac{\psi}{\bar{\Psi}_0'}\right|_{a=1}. \tag{2.5}$$

A numerical code, like ESC (Ref. [14]) can solve the linearized GSh Eq. (2.1) for each particular perturbation either of the plasma boundary or of the plasma profiles $\delta T, \delta P$. Then, the signals on diagnostics for each of N solutions ψ can be calculated in a straightforward way. The linear relationship between the vector $\vec{X}$ of coefficients of perturbation

$$\vec{X} \equiv \left\{ \underbrace{A_0, A_1, \ldots, A_{N_b-1}}_{N_\xi \ of \ \xi}, \underbrace{T_0, \ldots, T_{N_T-1}}_{N_T \ of \ \delta T}, \underbrace{P_0, \ldots, P_{N_P-1}}_{N_P \ of \ \delta P}, \right\} \tag{2.6}$$

and the vector $\delta\vec{S}$ of measured signals

$$\delta\vec{S} \equiv \left\{ \underbrace{\delta\Psi_0, \ldots, \delta\Psi_{M_\Psi-1}}_{M_\Psi \ of \ \delta\Psi}, \underbrace{\delta B_0, \ldots, \delta B_{M_B-1}}_{M_B \ of \ \delta B_{pol}}, \underbrace{\delta S_0, \ldots, \delta S_{M_S-1}}_{M_S \ of \ \textbf{others}} \right\} \tag{2.7}$$

can be written in matrix form:

$$\delta\vec{S} = \mathsf{A}\vec{X}, \quad \mathsf{A} = \mathsf{A}_{M\times N}, \quad M \equiv M_\Psi + M_B + M_S, \quad N \equiv N_\xi + N_J + N_P, . \tag{2.8}$$

Here, M_Ψ is the number of flux (saddle) loop signals, M_B is the number of signals from the local pickup coils, measuring poloidal magnetic field, M_S is the number of other signals (including the diamagnetic loop signal), MSE signals and all other signals used for equilibrium reconstruction, while M is the total number of signals. Typically $M > N$.

The response matrix A, calculated for a representative set of perturbations for a given magnetic configuration, is the final product of equilibrium calculations in the theory of variances. After this step, the analysis of the matrix problem (2.8) is applicable to other reconstruction problems, reduced to inversion of the response matrix.

3 Variances in equilibrium reconstruction *(to ToC)*

After calculation of the response matrix A, it is necessary to make a transition to a working matrix $\overline{\mathsf{A}}$, which weights each signal δS_m in accordance with its accuracy ϵ_m(assumed to be known *a priori*).

$$(\overline{\mathsf{A}})_m^{0\le n<N} \equiv \frac{1}{\epsilon_m}(\mathsf{A})_m^{0\le n<N}, \quad \delta\bar{S}_m \equiv \frac{1}{\epsilon_m}\delta S_m, \quad \overline{\mathsf{A}}\vec{X} = \delta\vec{\bar{S}}. \tag{3.1}$$

Then, using the Singular Value Decomposition (SVD) technique (Ref. [16]), the matrix $\overline{\mathsf{A}}$ should be presented as a product of three matrices

$$\overline{\mathsf{A}} = \mathsf{U}\cdot\mathsf{W}\cdot\mathsf{V}^T, \quad \mathsf{U} = \mathsf{U}_{M\times N},, \quad \mathsf{W} = \mathsf{W}_{N\times N}, \quad \mathsf{V} = \mathsf{V}_{N\times N} \tag{3.2}$$

where U is a rectangular matrix with orthogonal columns, normalized to unity,

$$\mathsf{U}^T\cdot\mathsf{U} = \mathsf{I}, \quad I_i^k = \delta_i^k, \tag{3.3}$$

I is the identity matrix, W is a diagonal matrix containing the eigen-values w^k of the problem

$$W_i^k = w^k\delta_i^k, \tag{3.4}$$

and the columns of V contain the normalized eigen-vectors of the problem

$$\mathsf{V}^T\cdot\mathsf{V} = \mathsf{I}, \tag{3.5}$$

as it is described in Ref. [16]. The expansion (3.2) is always possible and unique given the matrix $\overline{\mathsf{A}}$.

Each eigen-value, determined by this procedure, is associated with an eigen-vector $\vec{X}^k$ of coefficients (2.6), defined in terms of columns of the matrix V as

$$\vec{X}^k \equiv \gamma^k\mathsf{V}^k. \tag{3.6}$$

The factors γ^k scale each physical perturbation to the characteristic value of plasma perturbation $\xi_{max} \simeq 1$, or the current densities $\bar{\jmath}_{s,max}$, $\bar{\jmath}_{p,max}$ (whatever is the most limiting one).

Calculation of standard deviations (or Root Mean Square, RMS) of the signals $\delta\vec{\bar{S}}^k$ generated by each eigen-perturbation $\vec{X}^k$

$$\delta\vec{\bar{S}}^k = \overline{\mathsf{A}}\vec{X}^k = \gamma^k w^k\vec{U}^k, \quad \sqrt{\frac{1}{M}\sum_{m=0}^{m<M}\left(\delta\bar{S}_m^k\right)^2} = \frac{\gamma^k w^k}{\sqrt{M}}, \tag{3.7}$$

allows the introduction of variances $\bar{\sigma}^k$ in reconstruction of each eigen-perturbation as

$$\bar{\sigma}^k \equiv \frac{\sqrt{M}}{\gamma^k w^k}. \tag{3.8}$$

Variances $\bar{\sigma}^k$ in Eq.(3.8) specify uncertainties in the reconstruction of the plasma boundary ξ^k and current density $\delta T^k, \delta P^k$ for each eigen-perturbation in an explicit form, i.e.

$$\vec{X}^k \equiv \left\{ \underbrace{A_0^k, A_1^k, \ldots, A_{N_b-1}^k}_{N_\xi \ of \ \xi}, \underbrace{T_0^k, \ldots, T_{N_T-1}^k}_{N_T \ of \ \delta T}, \underbrace{P_0^k, \ldots, P_{N_P-1}^k}_{N_P \ of \ \delta P}, \right\}, \tag{3.9}$$
$$\xi^k = \bar{\sigma}^k \sum_{n=0}^{n<N_\xi} A_n^k \xi^n(\theta), \quad \delta T^k = \bar{\sigma}^k \sum_{n=0}^{n<N_J} T_n^k f^n(a), \quad \delta P^k = \bar{\sigma}^k \sum_{n=0}^{n<N_P} P_n^k f^n(a).$$

The amplitude of the uncertainties is proportional to the variances $\bar{\sigma}^k$. Because of normalization of the matrix equation (3.1), the characteristic value of $\bar{\sigma}^k = 1$ corresponds to a perturbation of the plasma boundary and current density in a magnetic configuration which is comparable to their background values, and still marginally visible by the diagnostics. The importance of variances $\bar{\sigma}^k$ is related to the following statement:

Perturbations $\vec{X}^k$ with $\bar{\sigma}^k > 1$, ($\log_{10} \bar{\sigma}^k > 0$) are essentially invisible to diagnostics with a given level of accuracy. The number of variances $\bar{\sigma}^k < 1$ in the spectrum of $\bar{\sigma}^k$, defined by Eq.(3.8), serves as a quantitative measure of quality of diagnostic systems for equilibrium reconstruction.

In this paper, the perturbations with (a) $\bar{\sigma}^k < 0.1$, $\log_{10} \bar{\sigma}^k < -1$ are qualified as "well detectable", with (b) $0.1 \leq \bar{\sigma}^k < 1$, $-1 \leq \log_{10} \bar{\sigma}^k < 0$ called "barely visible", and (c) with $1 \leq \bar{\sigma}^k$, $0 \leq \log_{10} \bar{\sigma}^k$ called "invisible".

The distinction between these 3 kinds of perturbations becomes obvious with the use $\sigma-$curves, which are plots of $\log_{10} \bar{\sigma}^k$ as function of k (assuming ascending ordering in σ^k). The intersection of the σ-curves with the zero level separates visible perturbations from those which cannot be reconstructed with a particular diagnostic system.

Based on explicit solution $\bar{\Psi}_0 + \psi^k$ of the linearized equilibrium equation for each eigen-perturbation, it is possible to calculate uncertainties in reconstruction of all physical quantities related to equilibrium, both local or integrated, e.g., q- and p-profiles, kinetic energy of the plasma, etc. Accordingly, it is possible to introduce variances of these quantities, e.g, $\bar{\sigma}_q^k, \bar{\sigma}_p^k$ for q- and p-profiles

$$\bar{\sigma}_q^k \equiv \sqrt{\int_0^1 (\delta q^k)^2 da} \propto \bar{\sigma}^k, \quad \bar{\sigma}_p^k \equiv \sqrt{\int_0^1 \left(\frac{\delta p^k}{p_{norm}} \right)^2 da} \propto \bar{\sigma}^k, \tag{3.10}$$

all proportional to basic variances $\bar{\sigma}^k$ (3.8). The variances in integrated quantities (like q- and p- profiles) are typically smaller than $\bar{\sigma}^k$, and they can be reconstructed with a better certainty than, e.g., the current density. In Eq. (3.10), p_{norm} is the normalization value of plasma pressure, suggested here as

$$p_{norm,MPa} \equiv \frac{I_{MA}^2}{20 S_{m^2}}. \tag{3.11}$$

This value corresponds to the average plasma pressure with $\beta_j = 1$ in Shafranov's definition

$$\beta_j = \frac{20 \int p_{MPa} dS_{m^2}}{I_{MA}^2}, \tag{3.12}$$

where I_{MA} is the plasma current, and S_{m^2} is the plasma poloidal cross-section.

Calculation of σ-curves for variances of physical quantities using the SVD technique solves the problem of uncertainties in a comprehensive way. The associated technique can be implemented into existing equilibrium reconstruction codes in order to generate information on variances remaining after equilibrium reconstruction has been performed.

4 Characteristic cases of reconstructions based on magnetic measurements *(to ToC)*

The ESC code [14] has been slightly modified in order to calculate w_k and variances in the current density, q- and p-profiles for different kinds of tokamak equilibria. They are presented in the order of complexity. In all examples the expansion functions $f^n(a)$ are taken in the trigonometric form (2.2) illustrated in Fig. 1b.

4.1 Shafranov's model of a circular plasma equilibrium *(to ToC)*

In the classical Shafranov model of equilibrium, only two harmonics of the poloidal magnetic field are present

$$B_{pol}(a,\theta) = B_0(a) + B_1^c(a)\cos\theta, \tag{4.1}$$

where both B_0 and B_1^c depend only on integral characteristics of the current density

$$B_0 = 2\pi\int_0^a \bar{\jmath}_s a da, \quad B_1^c = \frac{a}{R}\left(\beta_j + \frac{l_i}{2}\right), \quad \beta_j \equiv \frac{4}{a^2 B_0^2}\int_0^a (\bar{p} - \langle\bar{p}\rangle) a da, \quad l_i(a) \equiv \frac{1}{a^2 B_0^2}\int_0^a B_0^2 a da \tag{4.2}$$

inside the magnetic surface. Correspondingly, it is impossible the reconstruct the details of the current density except the total current and the combination $\frac{l_i}{2} + \beta_j$. The diamagnetic measurements, which are included into calculations, allow a distinction to be made between l_i and β_j.

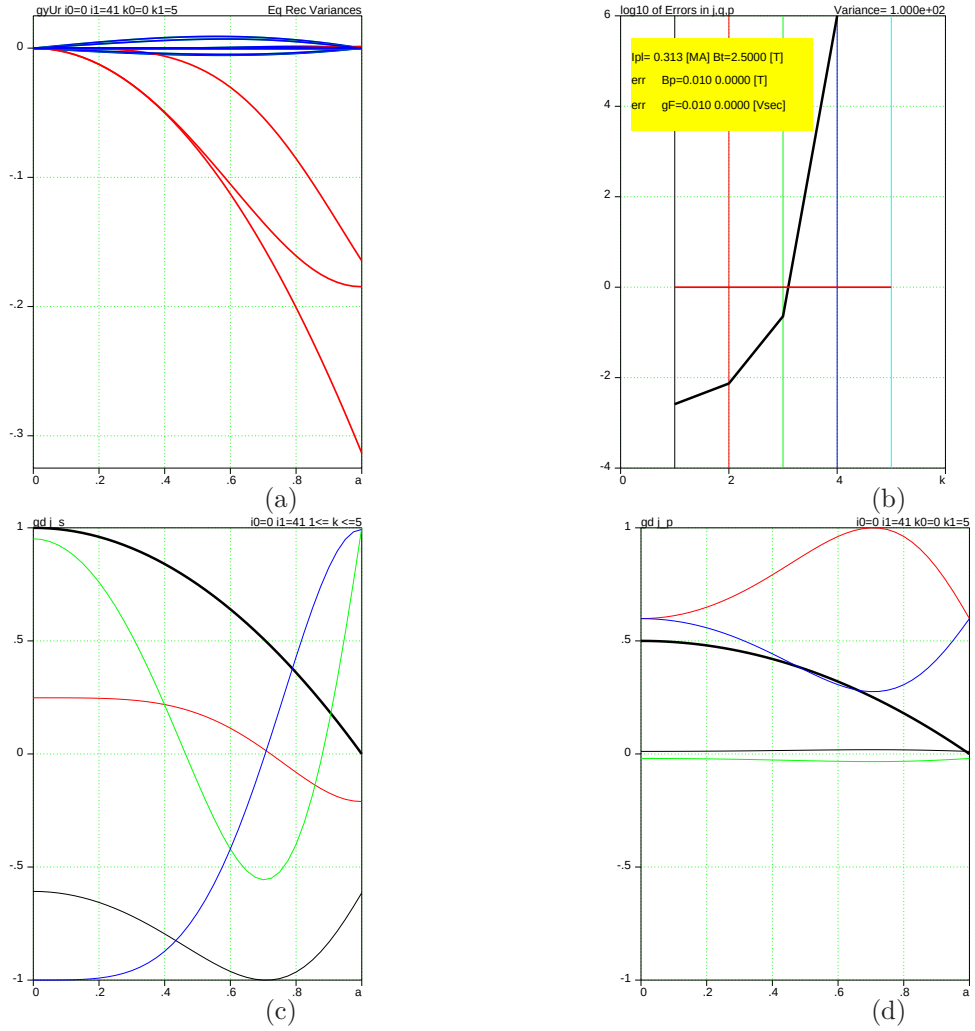

Figure 2: *(a) Amplitudes of Fourier harmonics* $\psi^k_m \cos m\theta$ *of four eigen-solutions* $\psi^k(a,\theta)$ *to the perturbed GSh equation (2.1) for Shafranov's model* ($N_J = 3$, $N_P = 2$). *Red color is used for* $\psi^k_{m=0}$ *and blue for all others,* $\psi^k_{m\neq 0}$. *(b)* σ*-curves* $\log_{10}\{\bar{\sigma}^k\}$. *The colors of vertical bars are used to specify the index* k *of eigen-values. (c) Normalized eigen-variances for* $\delta j^m_s(a)$ *as functions of* a. *The colors of functions corresponds to the colors of eigen-values. The thick black profile shows the background* $\bar{j}_s(a)$. *(d) The* $\delta j^m_s(a)$ *component of eigen-functions. The thick black profile shows the background* $\bar{j}_p(a)$.

For Shafranov's model only three well-known parameters of the magnetic configuration can be obtained for a full set of external magnetic measurements. Accordingly, the σ-curves in Fig.2 of the present theory of variances show only three meaningful eigen-values. (The fourth one was made artificially finite just for purposes of displaying the tendency).

4.2 Circular and non-circular cross sections *(to ToC)*

In this section the capacity of external magnetic diagnostics is described for different shapes of tokamak plasmas. All the figures are organized in the same manner for easy comparison. Initially, the plasma

configurations are shown.

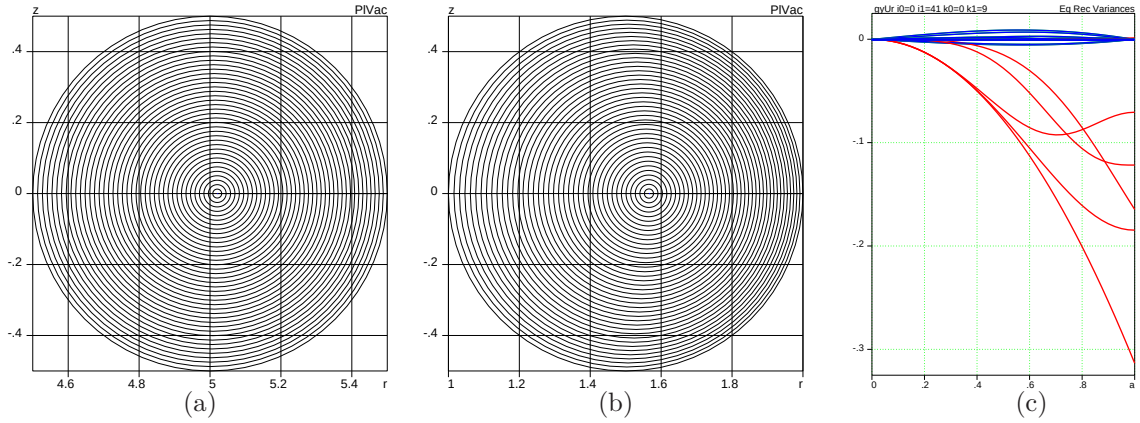

Figure 3: *Numerically obtained (using ESC) equilibrium configurations for circular cross-section plasmas: (a) large* $R/a_0 = 10$*, (b) medium* $R/a_0 = 3$ *aspect ratios equilibria, and (c) Fourier harmonics of eigen-solutions for* $R/a_0 = 3$ *and* $N_J = 5,\ N_P = 4$*.*

Then, the plots of (a) the basic σ^k-curves together with $\sigma^k_{q,p}$-curves for q- and p- profiles, variances for (b) q- and (c) p- profiles, (d) signals from variances (which fit the error bar range), and variances in (e) $\bar{j}_s$- and (f) $\bar{j}_p$-profiles are shown.

For simplicity, the relative error of all signals, i.e. B-coils and diamagnetic loop, is taken to be 0.01, while the absolute error in measurements is assumed to be 0.

We start with a circular plasma of a large aspect ratio $R/a = 10$ (Fig. 4), which is close to Shafranov's approximation. Similar to the Shafranov model, the σ-curves (calculated for σ, σ_q, σ_p) show that only 3 eigen-perturbations can be reconstructed by external magnetic measurements. The fourth one (blue curves) corresponds to variances of plasma profiles exceeding the background values.

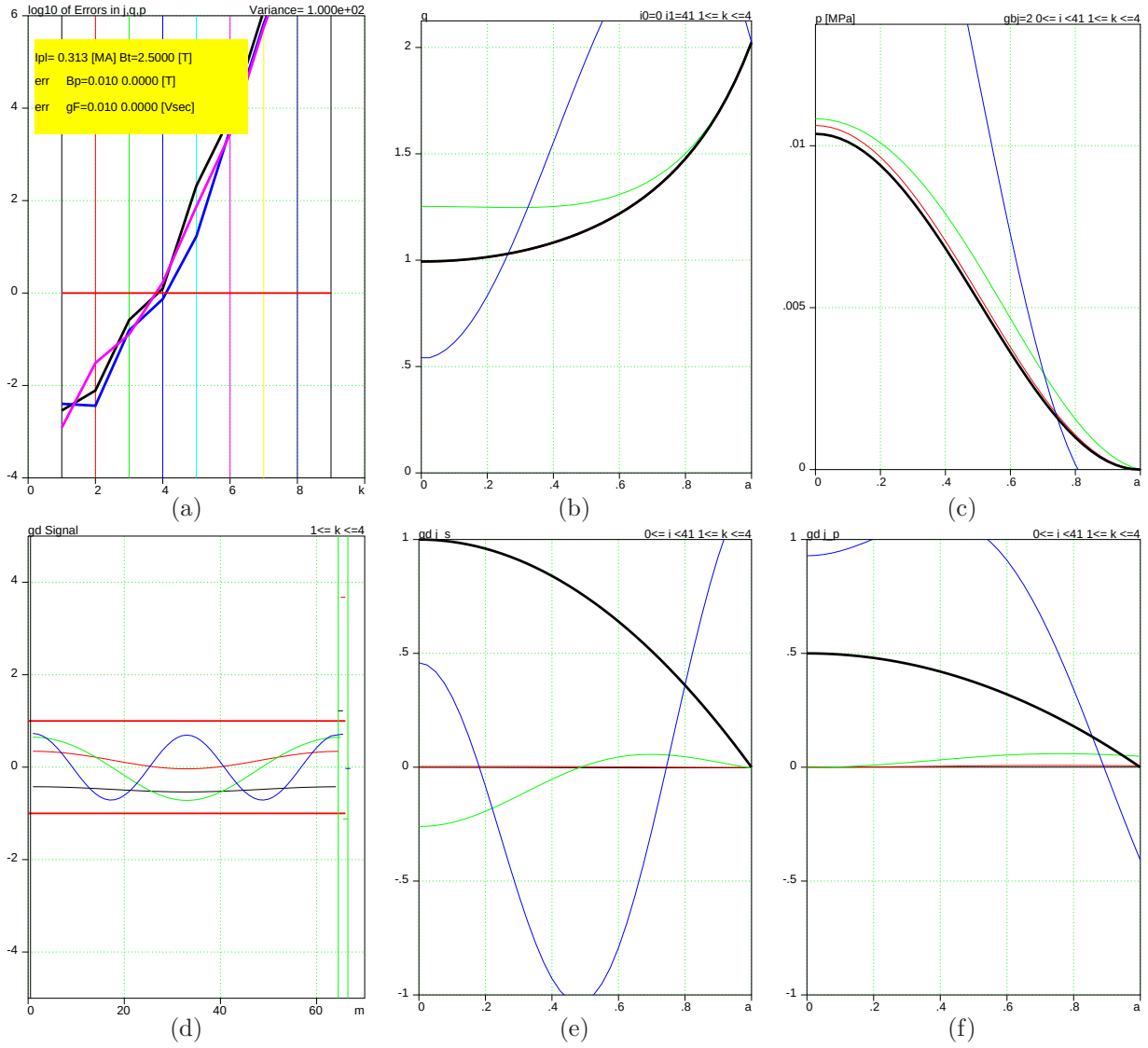

Figure 4: *The case of a fixed boundary circular plasma with a large aspect ratio, $R/a = 10$. (a) σ-curves $\log_{10}\{\bar{\sigma}^k,\ \bar{\sigma}_q^k,\ \bar{\sigma}_p^k\}$ for a diagnostic system using B-coils and a diamagnetic Φ-loop. (b) q-profile (thick black curve) and q-profiles modified by variances corresponding to four first eigen-solutions. (c) the same for the pressure p-profile. (d) The signals from variances on 64 B-coils and one Φ-loop. The red horizontal lines specify the range of detectability of the signals. (e) Background $\bar{\jmath}_s$-profile (thick black curve) and variances in the $\bar{\jmath}_s$ profile, normalized to the level of their visibility. (f) The same for the $\bar{\jmath}_p$-profile.*

Reduction of the aspect ratio to the level $R/a = 10$ (Fig. 5) makes the situation slightly better, i.e. four eigen-perturbations can be reconstructed. The fifth one (cyan color) displays unacceptable variances despite the fact that the signals from it are smaller than the detectable level.

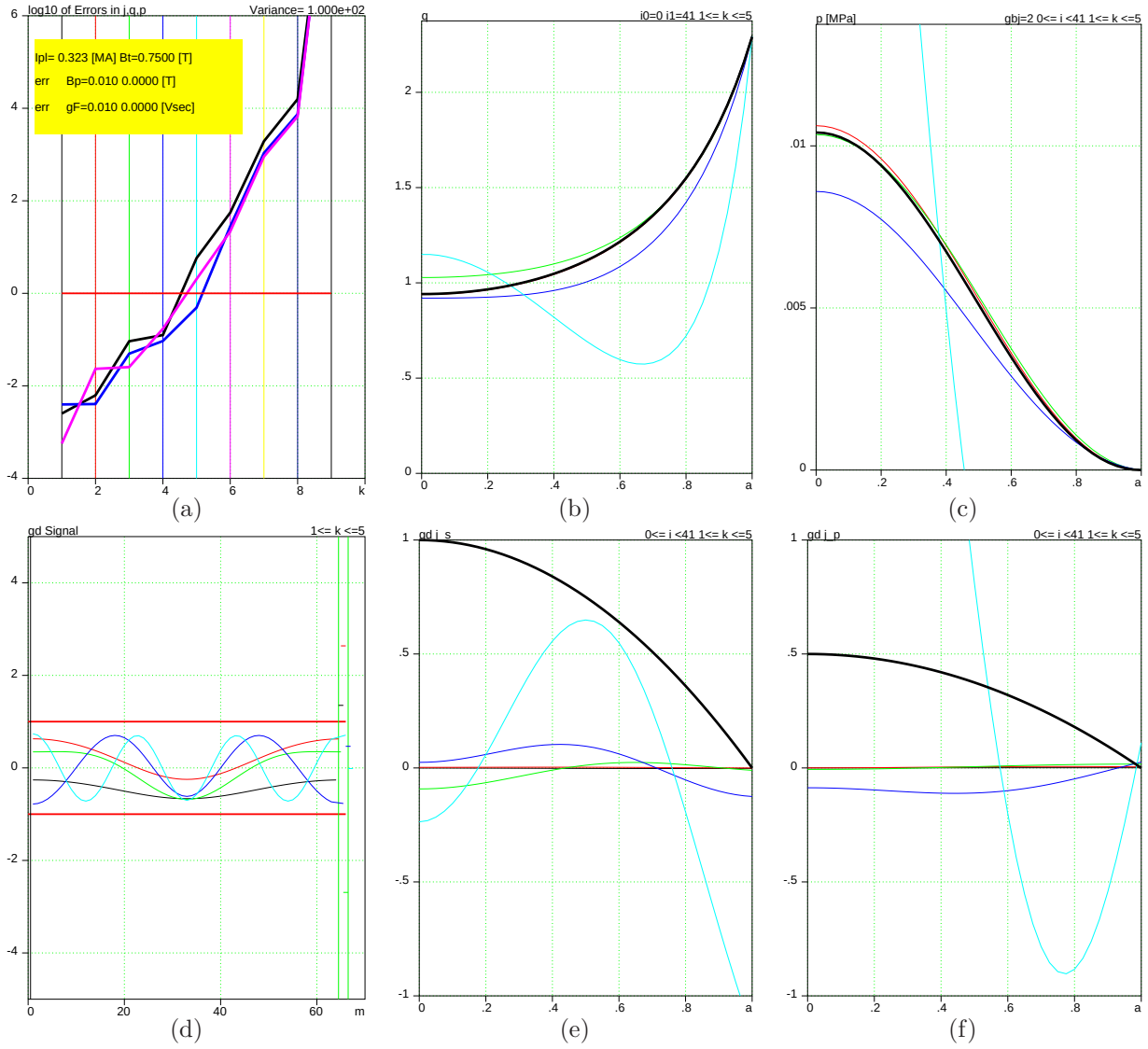

Figure 5: *The case of a fixed boundary circular plasma with a modest aspect ratio, $R/a = 3$ with (a) σ-curves* $\log_{10}\{\bar{\sigma}^k,\ \bar{\sigma}_q^k,\ \bar{\sigma}_p^k\}$ *for a diagnostic system using B-coils and a diamagnetic Φ-loop. (b) q-profile (thick black curve) and q-profiles modified by variances corresponding to four first eigen-solutions. (c) the same for the pressure p-profile. (d) The signals from variances on 64 B-coils and one Φ-loop. The red horizontal lines specify the range of detectability of the signals. (e) Background $\bar{\jmath}_s$-profile (thick black curve) and variances in the $\bar{\jmath}_s$ profile, normalized to the level of their visibility. (f) The same for the $\bar{\jmath}_p$-profile.*

4.3 Non-circular cross-sections *(to ToC)*

The transition to non-circular cross-sections extends the number of visible eigen-perturbations. Two simple non-circular magnetic configurations are shown in Fig. 6.

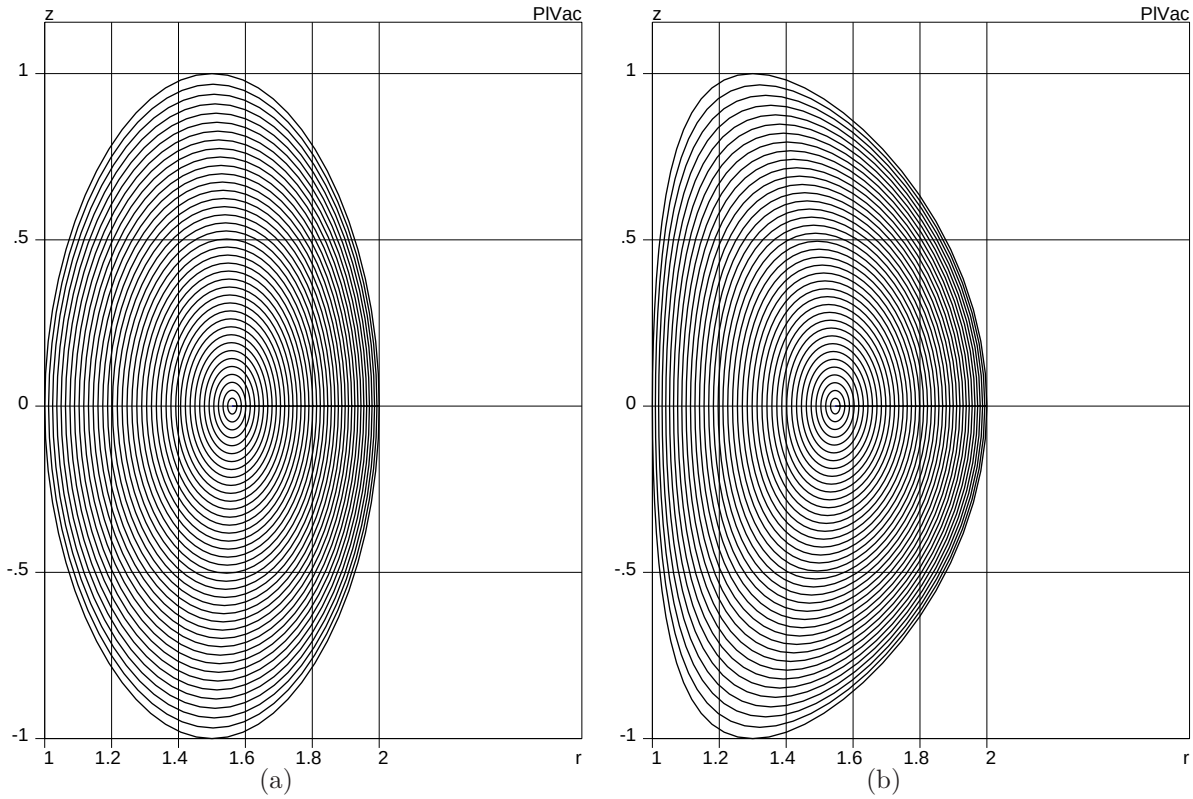

Figure 6: *Numerically obtained (using ESC) equilibrium configurations for non-circular cross-section plasmas, large* $R/a_0 = 3$*, elongation* $\kappa = 2$*: (a) elliptical cross-section (b) D-shaped cross-section.*

The $\sigma-$curves in Fig. 7 shows that for the case of the elliptical cross-section, the number of visible perturbations is enhanced to $k = 7$.

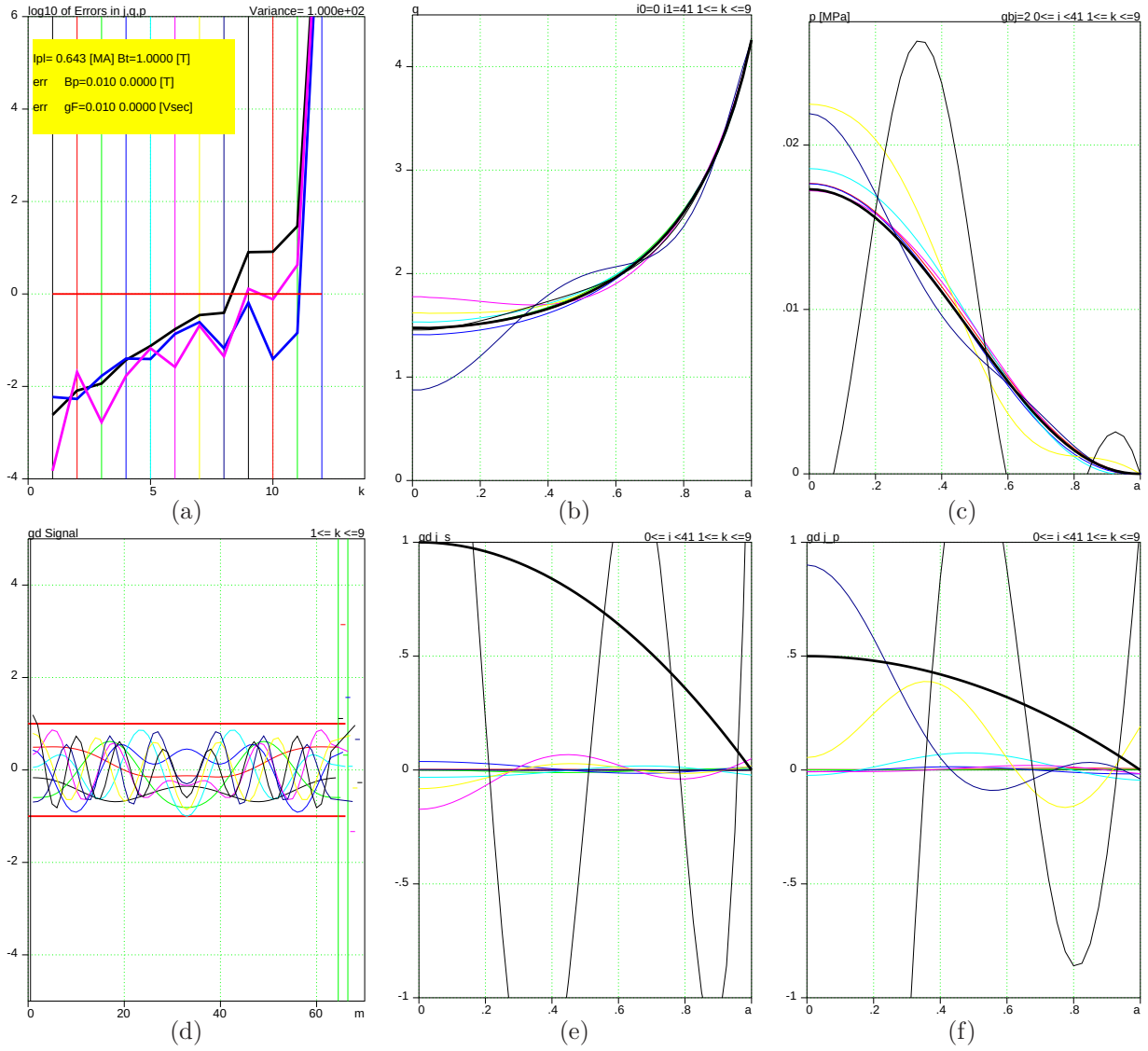

Figure 7: *The case of a fixed boundary plasma with $R/a = 3$, $\kappa = 2$ with elliptical cross-section. (a) σ-curves $\log_{10}\{\bar{\sigma}^k,\ \bar{\sigma}^k_q,\ \bar{\sigma}^k_p\}$ for a diagnostic system using B-coils and a diamagnetic Φ-loop. (b) q-profile (thick black curve) and q-profiles modified by variances corresponding to the first eight eigen-solutions. (c) the same for the pressure p-profile. (d) The signals from variances on 64 B-coils and one Φ-loop. The red horizontal lines specify the range of detectability of the signals. (e) Background $\bar{j}_s$-profile (thick black curve) and variances in the $\bar{j}_s$ profile, normalized to the level of their visibility. (f) The same for the $\bar{j}_p$-profile.*

The shaping of the elongated plasma (Fig. 8) does not affect the range of visible perturbations. As in the previous case, the variances for $k = 8$ are unacceptable.

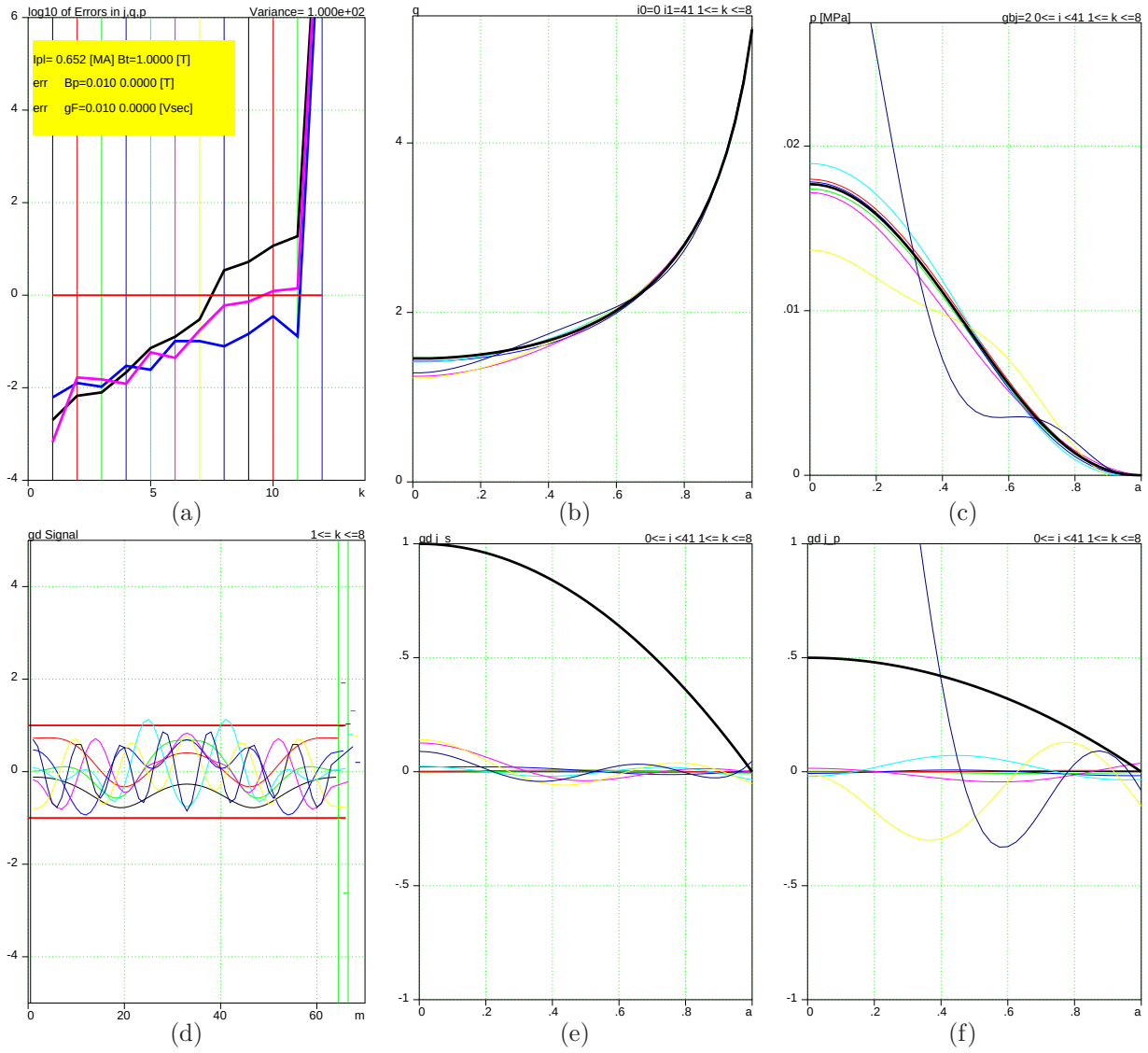

Figure 8: *The case of a fixed boundary plasma with $R/a = 3$, $\kappa = 2$ with D-shaped cross-section. (a) σ-curves* $\log_{10}\{\bar{\sigma}^k,\ \bar{\sigma}^k_q,\ \bar{\sigma}^k_p\}$ *for a diagnostic system using B-coils and a diamagnetic Φ-loop. (b) q-profile (thick black curve) and q-profiles modified by variances corresponding to the first eight eigen-solutions. (c) the same for the pressure p-profile. (d) The signals from variances on 64 B-coils and one Φ-loop. The red horizontal lines specify the range of detectability of the signals. (e) Background $\bar{j}_s$-profile (thick black curve) and variances in the $\bar{j}_s$ profile, normalized to the level of their visibility. (f) The same for the $\bar{j}_p$-profile.*

Nevertheless, comparison of the two cases (Figs. 7,8) shows that with the D-shaped plasma reconstruction of the q-profile can be much better than for a simple elliptic configuration.

4.4 Spherical tokamaks *(to ToC)*

Spherical tokamaks (ST) play a special role in fusion, because of their compactness and high beta. Also, they can benefit from elongation, D-shaping and reduced aspect ratio. In Fig.9, two ST cross-sections are shown. The first one is up-down symmetric, while the second one has different triangularities on the top and bottom.

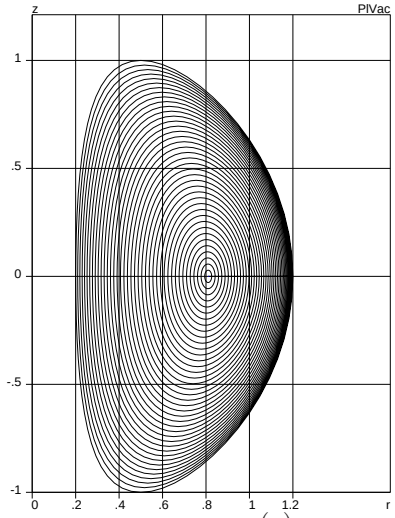

(a)

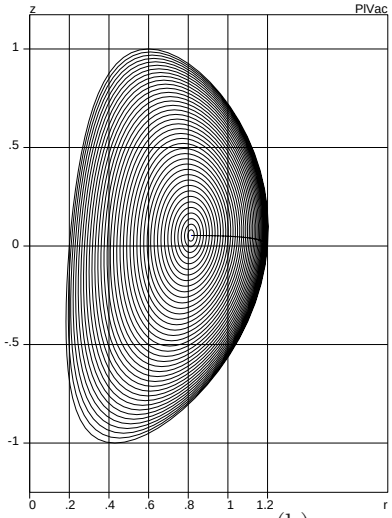

(b)

Figure 9: *Equilibrium configurations for spherical tokamak plasmas,* $R/a_0 = 1.4$*, elongation* $\kappa = 2$ *and low beta: (a) up-down symmetric case (b) up-down asymmetric case.*

The σ-curves in Fig.10 indicate that while the spectrum of the visible perturbations remains the same $k < 8$, the q-profile of spherical tokamaks is better reconstructed than the pressure.

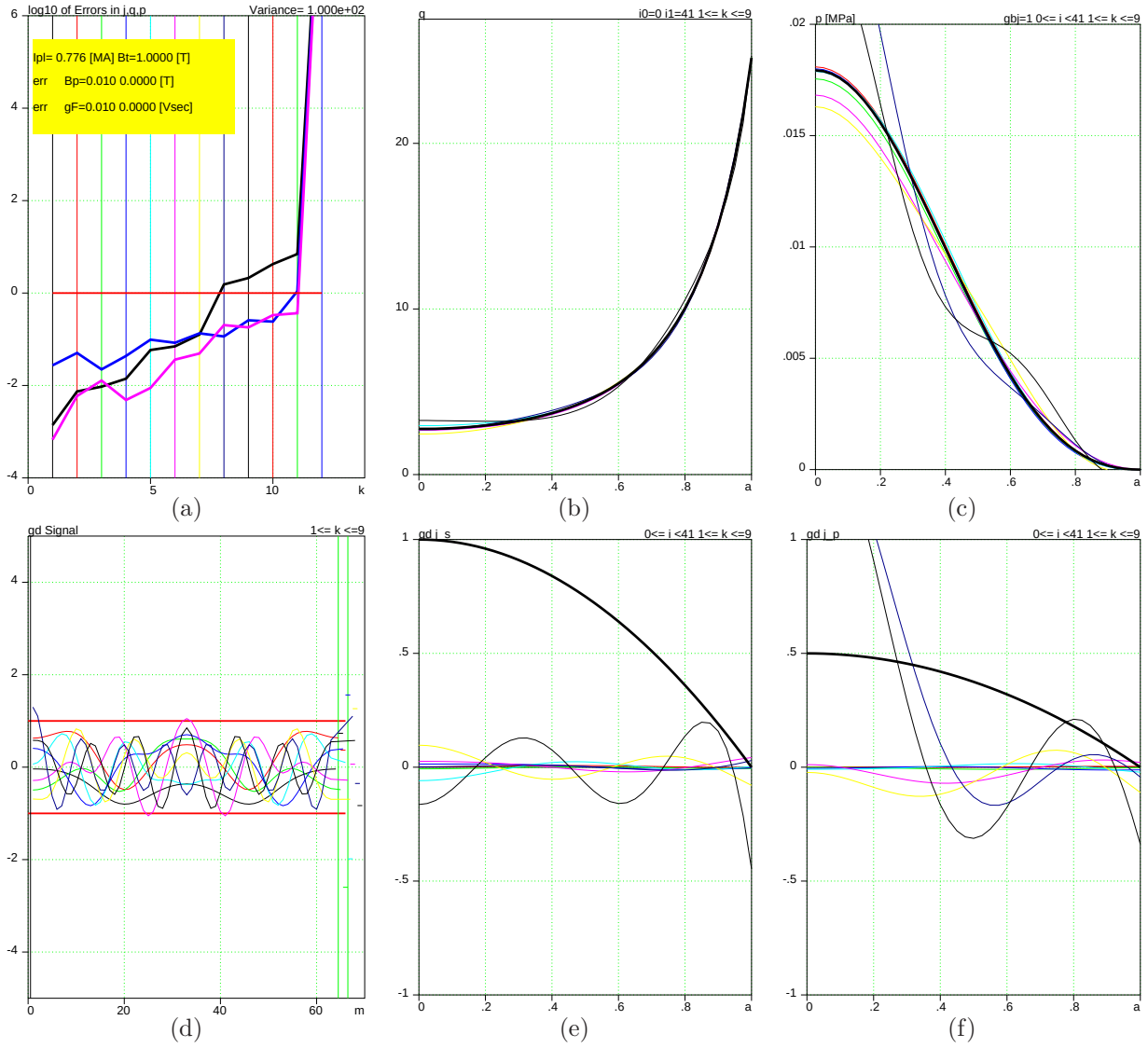

Figure 10: *The case of a up-down symmetric fixed boundary plasma of a spherical tokamak with* $R/a = 1.4$, $\kappa = 2$. *(a)* σ*-curves* $\log_{10}\{\bar{\sigma}^k,\ \bar{\sigma}_q^k,\ \bar{\sigma}_p^k\}$ *for a diagnostic system using* B*-coils and a diamagnetic* Φ*-loop. (b)* q*-profile (thick black curve) and* q*-profiles modified by variances corresponding to the first eight eigensolutions. (c) the same for the pressure* p*-profile. (d) The signals from variances on 64* B*-coils and one* Φ*-loop. The red horizontal lines specify the range of detectability of the signals. (e) Background* $\bar{\jmath}_s$*-profile (thick black curve) and variances in the* $\bar{\jmath}_s$ *profile, normalized to the level of their visibility. (f) The same for the* $\bar{\jmath}_p$*-profile.*

Asymmetry with respect to the mid plane only slightly improves the situation as is shown in Fig.11.

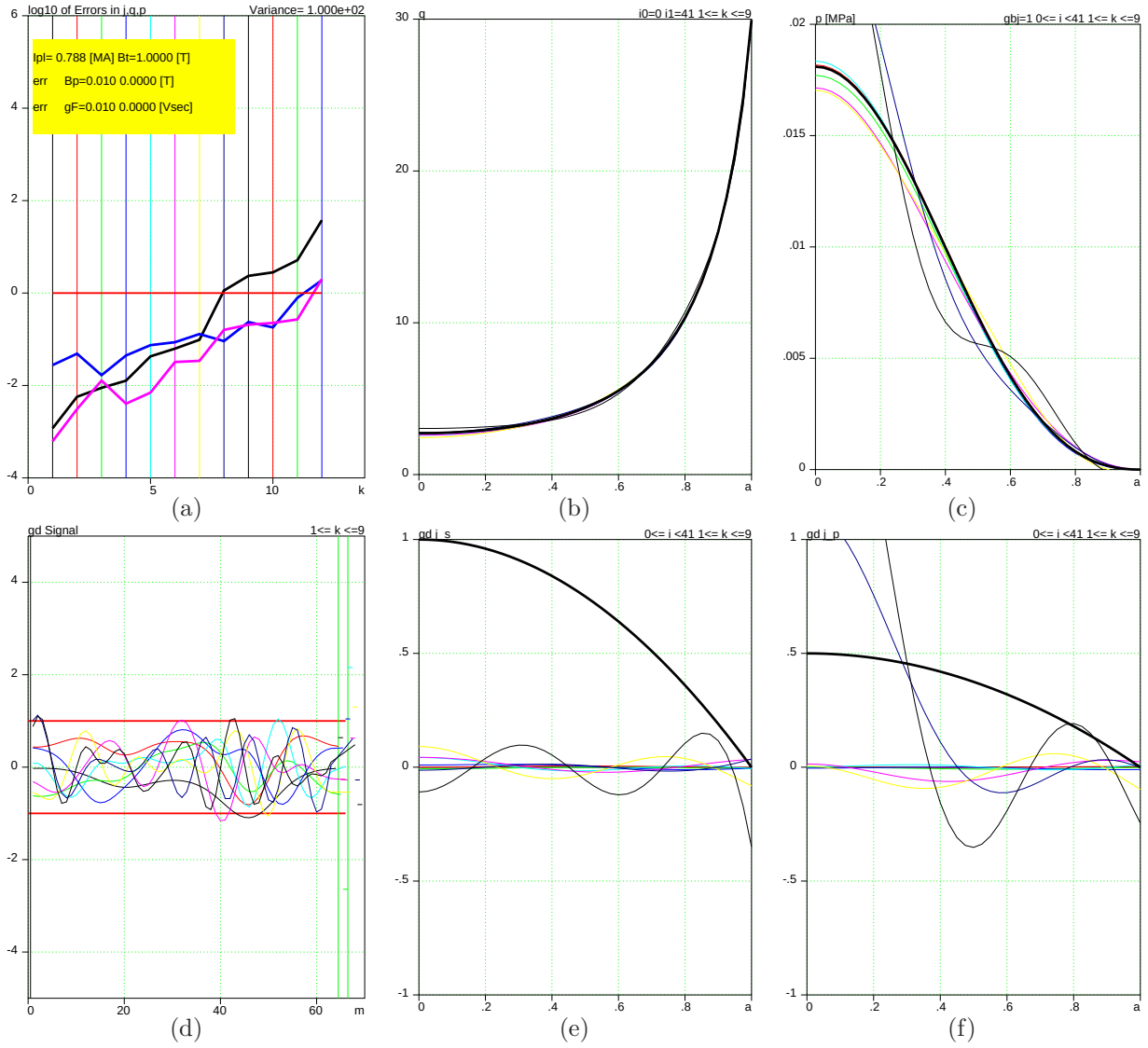

Figure 11: *The case of an up-down asymmetric fixed boundary plasma of a spherical tokamak with* $R/a = 1.4$, $\kappa = 2$. *(a)* σ*-curves* $\log_{10}\{\bar{\sigma}^k,\ \bar{\sigma}^k_q,\ \bar{\sigma}^k_p\}$ *for a diagnostic system using* B*-coils and a diamagnetic* Φ*-loop. (b)* q*-profile (thick black curve) and* q*-profiles modified by variances corresponding to the first eight eigen-solutions. (c) the same for the pressure* p*-profile. (d) The signals from variances on 64* B*-coils and* Φ*-loop. The red horizontal lines specify the range of detectability of the signals. (e) Background* $\bar{\jmath}_s$*-profile (thick black curve) and variances in the* $\bar{\jmath}_s$ *profile, normalized to the level of their visibility. (f) The same for the* $\bar{\jmath}_p$*-profile.*

4.5 High β and non-monotonic current density *(to ToC)*

Now, two configurations with different $\bar{\jmath}_s, \bar{\jmath}_p$ profiles are discussed. One of them (Fig. 12a) corresponds to a high $\beta = 0.35$, while another (Fig. 12b) represents the case of non-monotonic q-profile.

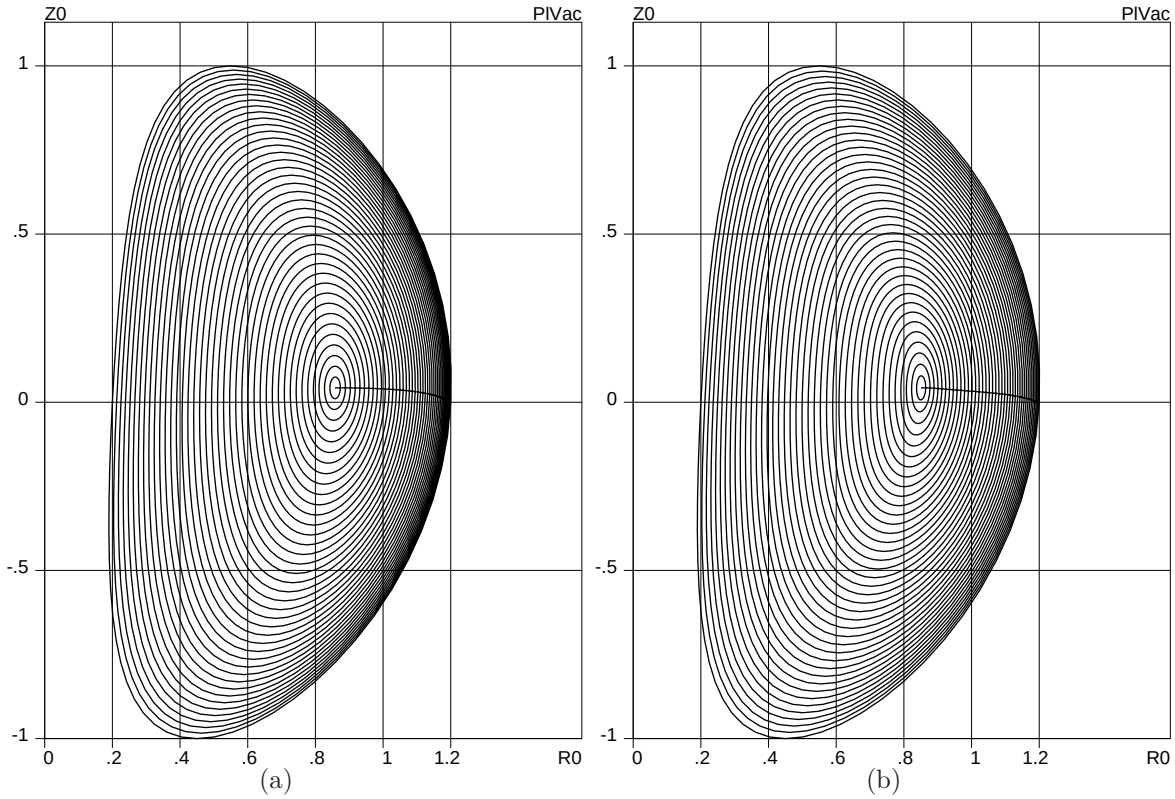

Figure 12: *Equilibrium configurations for a spherical tokamak plasmas,* $R/a_0 = 1.4$*, elongation* $\kappa = 2$*: (a) high* $\beta = 0.35$ *configuration, (b) moderate* $\beta = 0.14$ *with a non-monotonic current density profile.*

For both cases, the spectrum of visible perturbations remains the same as before ($k < 8$). Nevertheless the relative accuracy of reconstruction of the pressure profile was significantly improved for the high beta case in Fig. 13. At the same time, the variance in the q-profile reconstruction became larger.

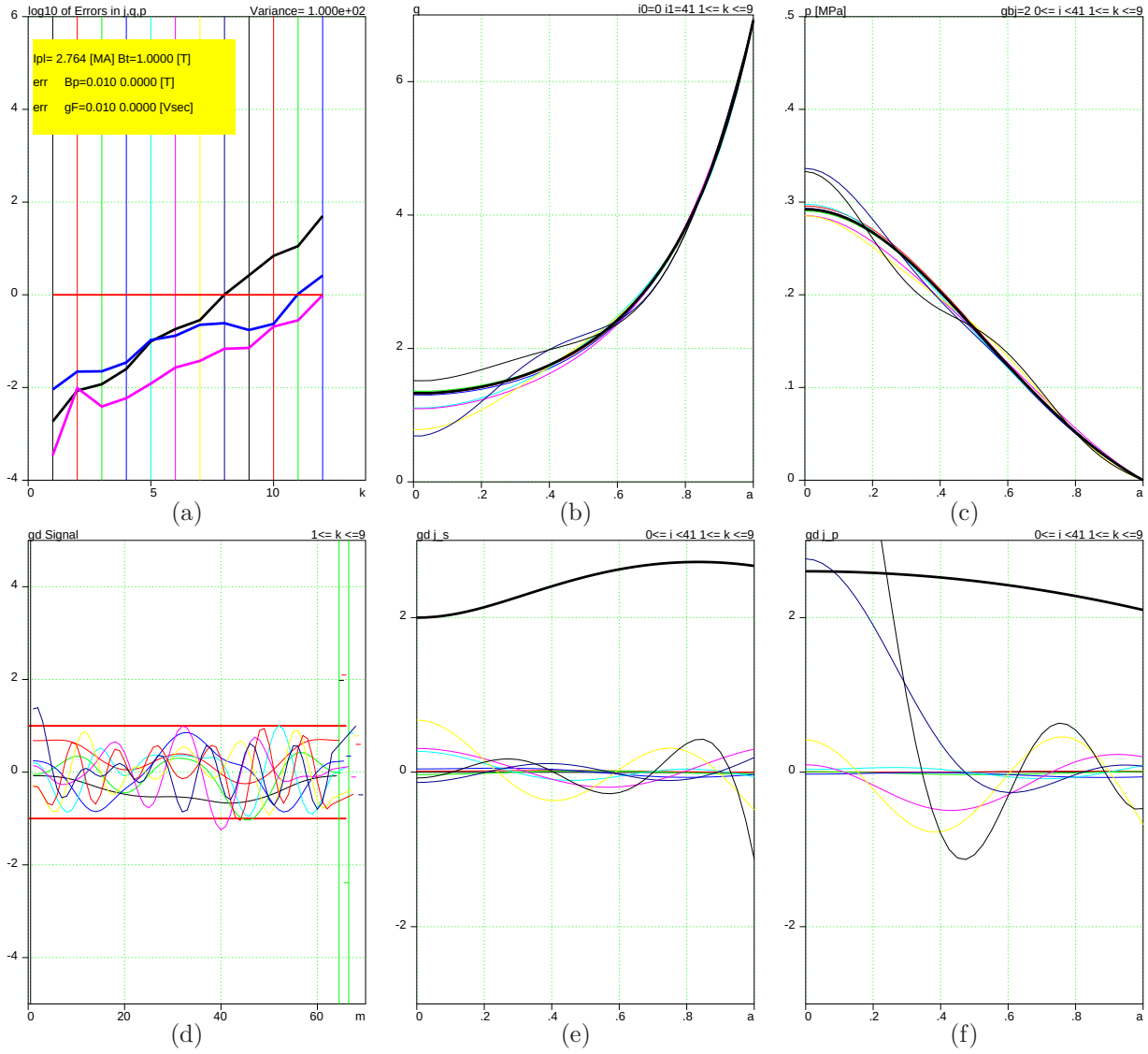

Figure 13: *The case of a up-down asymmetric fixed boundary plasma of a spherical tokamak with* $R/a = 1.4$, $\kappa = 2$ *and high* $\beta = 0.35$. *(a)* σ*-curves* $\log_{10}\{\bar{\sigma}^k,\ \bar{\sigma}^k_q,\ \bar{\sigma}^k_p\}$ *for a diagnostic system using* B*-coils and a diamagnetic* Φ*-loop. (b)* q*-profile (thick black curve) and* q*-profiles modified by variances corresponding to the first eight eigen-solutions. (c) the same for the pressure* p*-profile. (d) The signals from variances on 64* B*-coils and one* Φ*-loop. The red horizontal lines specify the range of detectability of the signals. (e) Background* $\bar{\jmath}_s$*-profile (thick black curve) and variances in the* $\bar{\jmath}_s$ *profile, normalized to the level of their visibility. (f) The same for the* $\bar{\jmath}_p$*-profile.*

Fig. 14 indicates that the variances in reconstruction of the non-monotonic current density profiles are esentially the same as for the monotonic case.

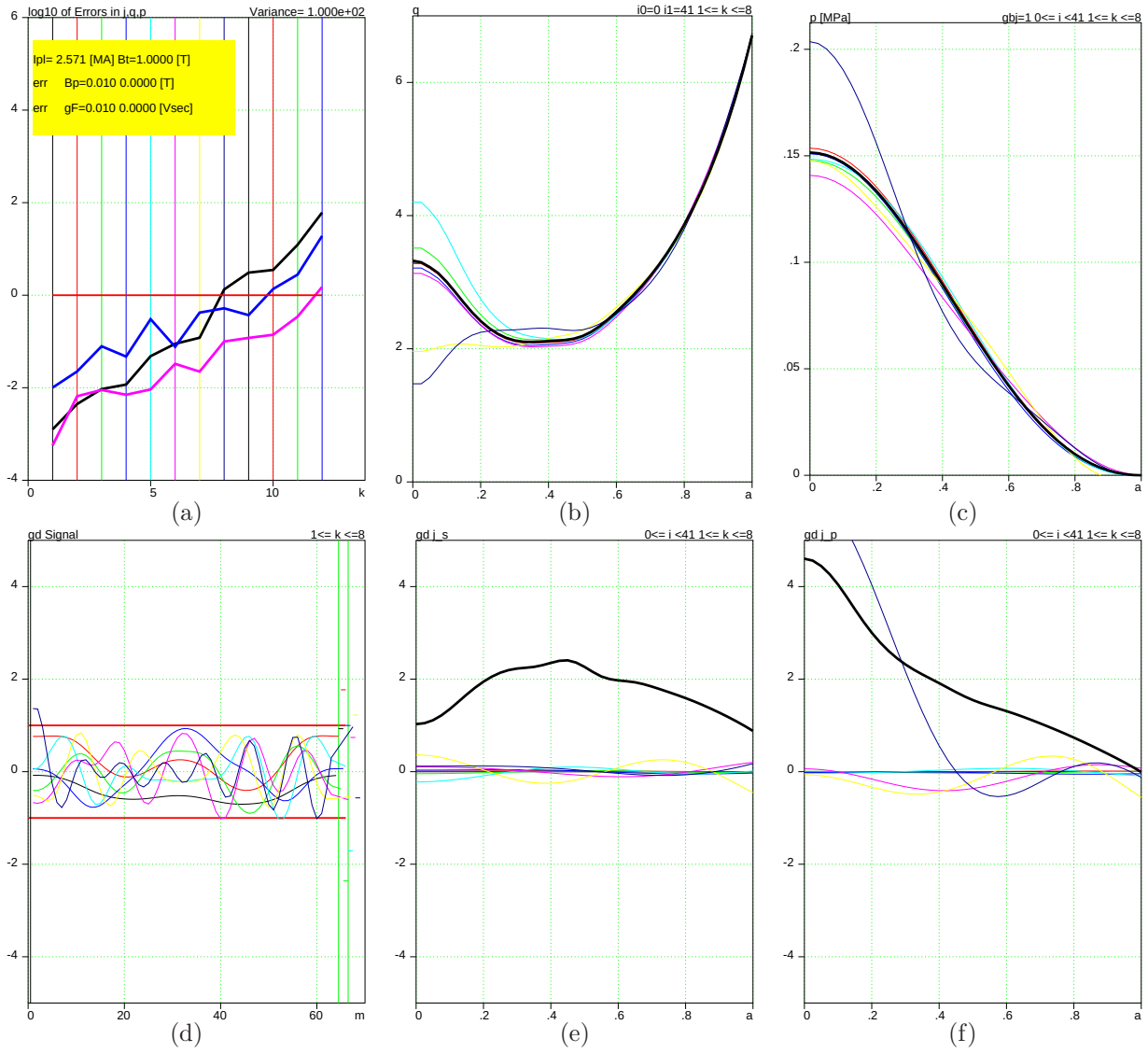

Figure 14: *The case of an up-down asymmetric fixed boundary plasma of a spherical tokamak with* $R/a = 1.4$, $\kappa = 2$ *and* $\beta = 0.14$ *and non-monotonic current density profile. (a)* σ*-curves* $\log_{10}\{\bar{\sigma}^k,\ \bar{\sigma}^k_q,\ \bar{\sigma}^k_p\}$ *for a diagnostic system using* B*-coils and a diamagnetic* Φ*-loop. (b)* q*-profile (thick black curve) and* q*-profiles modified by variances corresponding to the first eight eigen-solutions. (c) the same for the pressure* p*-profile. (d) The signals from variances on 64* B*-coils and one* Φ*-loop. The red horizontal lines specify the range of detectability of the signals. (e) Background* $\bar{\jmath}_s$*-profile (thick black curve) and variances in the* $\bar{\jmath}_s$ *profile, normalized to the level of their visibility. (f) The same for the* $\bar{\jmath}_p$*-profile.*

5 Possibility of complete reconstruction with internal measurements *(to ToC)*

This section illustrates the effect of internal measurements on equilibrium reconstruction. As an example, an ITER configuration with the plasma current $I_{pl} = 15$ MA is considered, where the external magnetic

diagnostics are complemented by MSE measurements.

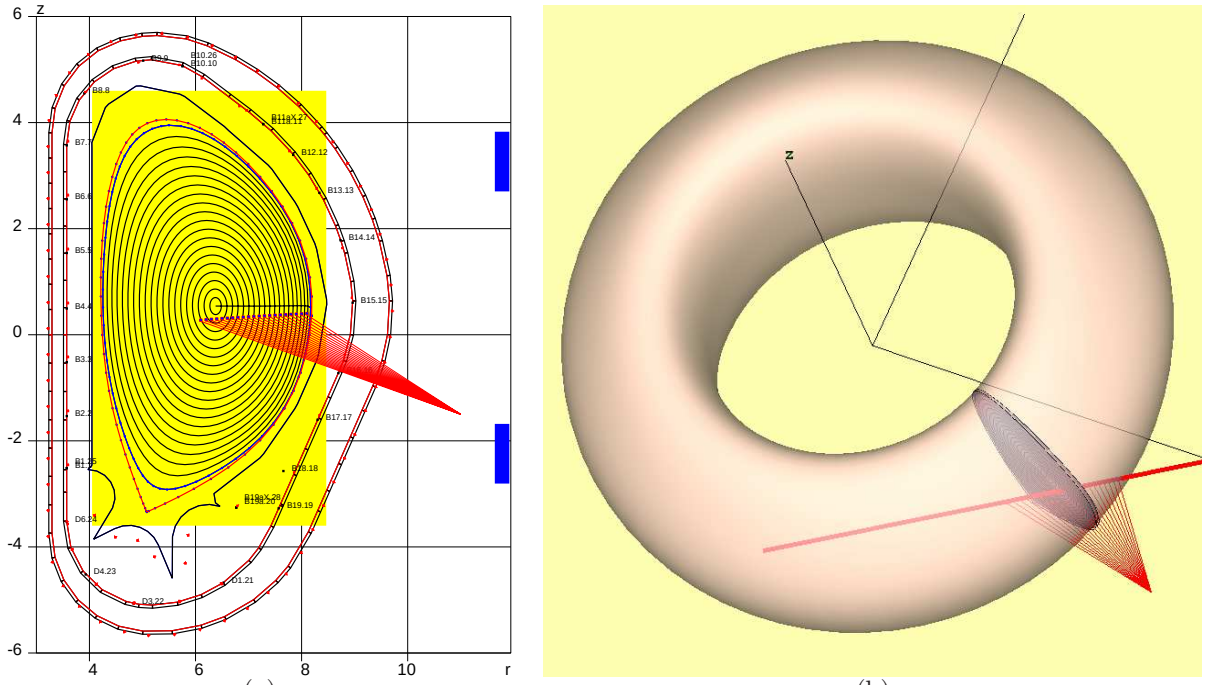

(a) (b)

Figure 15: Illustrative set of diagnostics for equilibrium reconstruction in ITER (a) ITER plasma cross-sections with 32 Ψ-loops, one Φ diamagnetic loop, 64 B-pickup coils, and 21 pickup points of MSE (b) Center line of 1 MeV NBI in ITER for collecting the MSE data

In this illustrative set of diagnostics, with no attempt to simulate the real one, it was assumed that the magnetic measurements are collected from vicinity of the plasma boundary. The accuracies ϵ of signals have been prescribed as shown in Table 1.

Signal name	$\epsilon^{relative}$	$\epsilon^{absolute}$	Comment **Table 1**
B-coils	0.01	0.01 T	local pickup coils
Ψ-loops	0.01	0.001 Vsec	local value of the poloidal flux
Φ-loop	0.01	0.001 Vsec	diamagnetic loop signal
MSE-LP	0.01	0.1^o	B_z/B_φ from the line polarization signal MSE-LP
MSE-LS	0.01	0.05 T	$\sqrt{\lvert\mathbf{B}\rvert^2-(\mathbf{B}\cdot\mathbf{v})^2}$ from the line shift signal MSE-LS

Two types of MSE signals are considered, the Stark line polarization signal (MSE-LP), providing the information on the pitch angle of the magnetic field line, and the Stark line shift signal (MSE-LS). Giving the quantity $\sqrt{|\mathbf{B}|^2-(\mathbf{B}\cdot\mathbf{v})^2}$ related to the magnetic field magnitude, where $\mathbf{v}$ is the unit vector along the neutral beam, it may be possible to use MSE-LS on ITER because of the high energy neutral beam (1 MeV) and high value of the magnetic field $B_\varphi \simeq 5.6$ T [15].

MSE-LP and MSE-LS signals were assumed to be pointwise. In reality a spacially distributed model of these signal is necessary.

The following examples demonstrate the effect of external and internal measurements on reconstruction of the current density, q, and p-profiles. Use of different combinations of signals results in different residual variances.

In most of the examples in this section, the plasma boundary is assumed to be well specified, while other signals, Φ-loop, B-coils and MSE are used for reconstruction of the current distribution. The effect of

plasmas boundary reconstruction is illustrated at the end of the section.

5.1 Variances in reconstruction with Φ-loop, B-coil signals for fixed plasma boundary *(to ToC)*

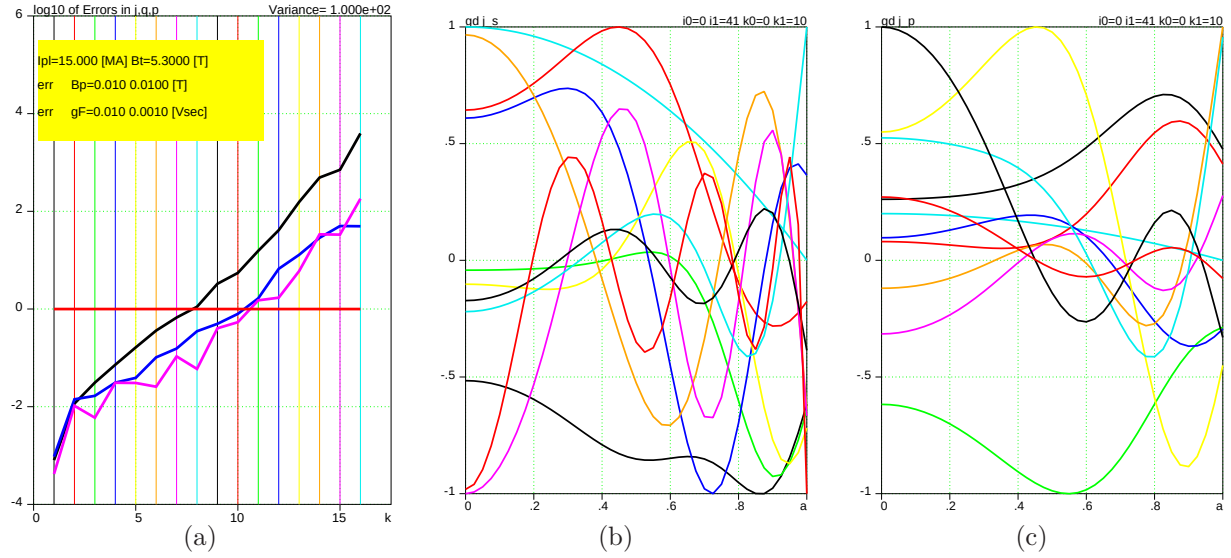

(a) (b) (c)

Figure 16: *(a) σ-curves* $\log_{10}\{\bar\sigma^k, \bar\sigma^k_q, \bar\sigma^k_p\}$ *for* $\xi = 0$ *and* ($N_J = 8$, $N_P = 8$). *The relative and absolute accuracy of signals, used in reconstruction, is specified in the yellow box. (b) Eigen-perturbations* $\delta j^k_s(a)$. *(c) Eigen-perturbations* $\delta j^k_p(a)$, $j_p \equiv P/R_0$. *The color of eigen-perturbations corresponds to the color of the index* k.

In Fig. 16a, $\log_{10}\bar\sigma_q$ and $\log_{10}\bar\sigma^k_p$ (where $\bar\sigma^k_p$ are normalized to 1 [MPa]) are the σ-curves for the q- and p-profiles. Eigen-perturbations $j^{k>8}_s, j^{k>8}_p$, corresponding to $\log_{10}\bar\sigma > 0$ are invisible in diagnostics and cannot be reconstructed.

In practice, a very restricted number, like $N_J{+}N_P \le 5$, of expansion functions is typically used in reconstruction, in order to provide stability of an iterative solution of the GSh equation. Testing variances using the same limited set of perturbations can produce a very good result, as in Fig. 17.

In fact, even a slight extension of the spectrum of perturbations from $N = 5$ to $N = 7, 8$, as in Figs. 18,19 shows that the variances could be noticeable. At the same time, the plots Figs. 18c,19c show that the amplitude of the signals from perturbations is undetectable by diagnostics, making the reconstruction doubtful.

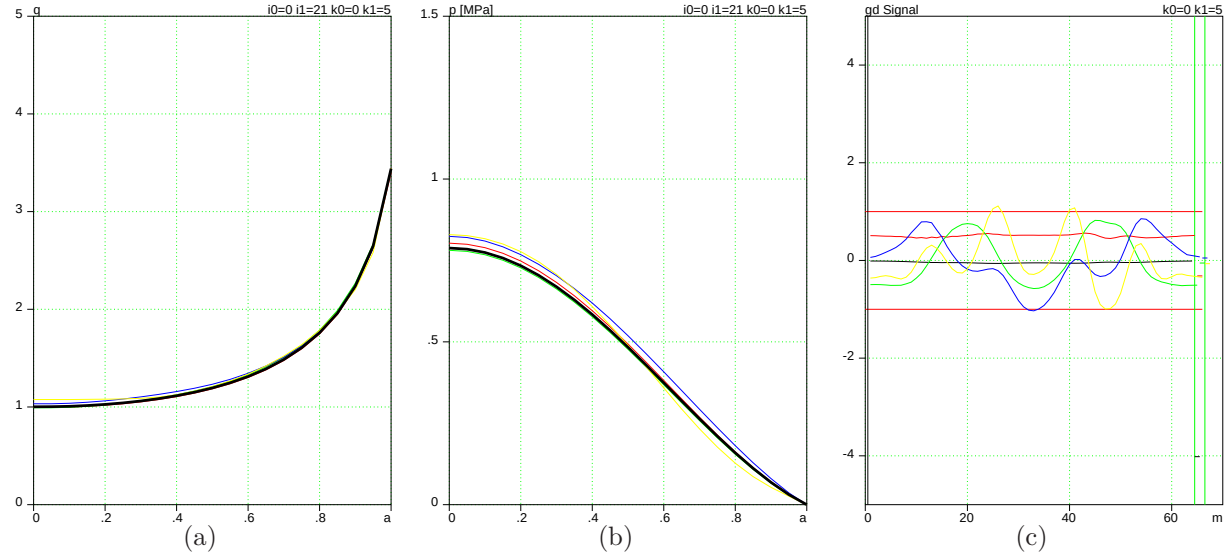

Figure 17: *Variances in (a) q and (b) p-profiles as functions of a in the range $k_J \leq 3$, $k_P \leq 2$. (c) Normalized signals $\delta\bar{S}_m = \delta S_m/\epsilon_m$ generated by the eigen-perturbations on the B-coils ($0 \leq m < 64$) and Φ-loop ($m = 64$). The horizontal lines $\delta\bar{S}_m = \pm 1$ specify the range of "invisible" signals $|\delta S_m| < \epsilon_m$.*

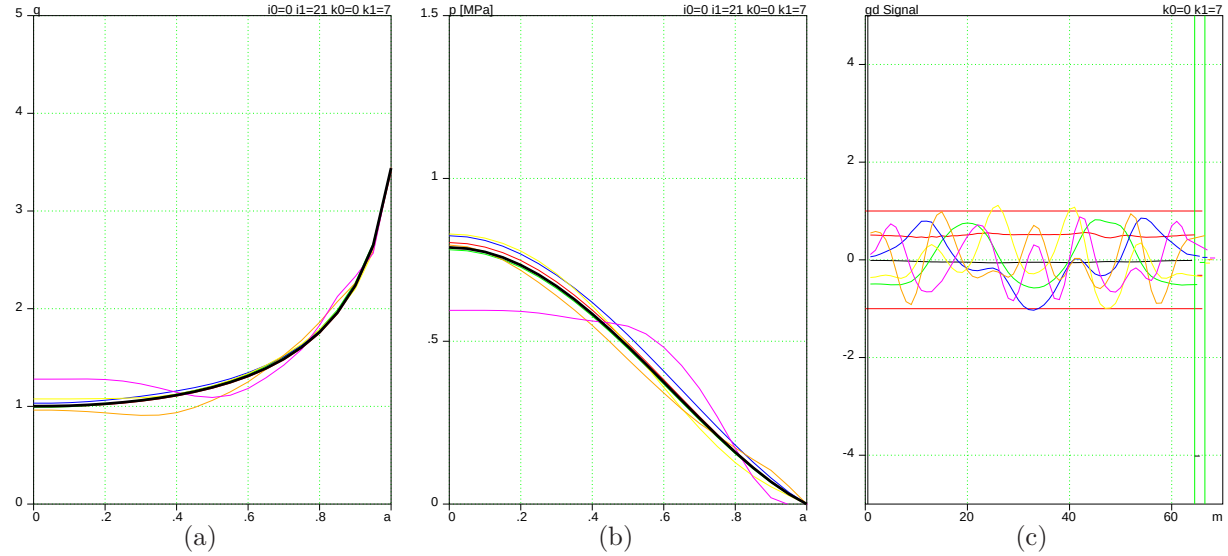

Figure 18: *Same variances and signals as in Fig. 17 but in an extended range $k_J \leq 4$, $k_P \leq 3$.*

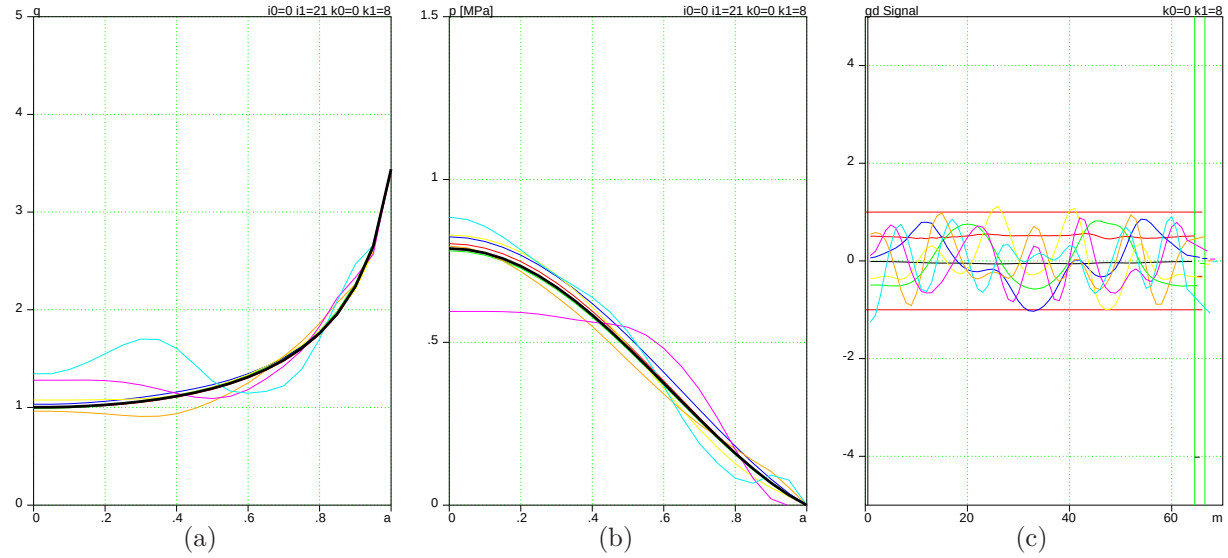

Figure 19: *Same variances and signals as in Fig. 18 but in the larger range* $k_J \leq 4$, $k_P \leq 4$.

A test of the full spectrum (Fig. 20), k_J+k_P=16, used in this paper for current density perturbations, shows that with no internal measurements constraints the variances are enormous and the reconstruction has no scientific value.

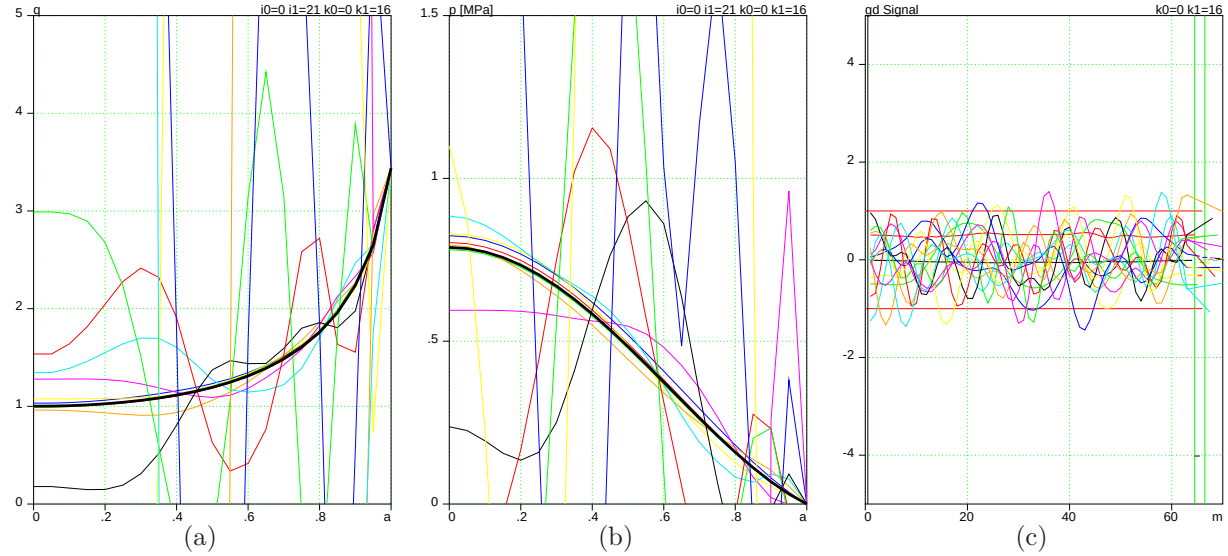

Figure 20: *Same variances and signals as in Fig. 18,19 but in full range* $k_J \leq 8$, $k_P \leq 8$.

5.2 Effect of MSE-LP signals on variances in reconstruction *(to ToC)*

The behavior of the σ-curves as a function of the index k for a reconstruction based on external magnetic measurements clearly indicates that even for non-circular plasma cross-sections it is not possible to get a good reconstruction of q- and p-profiles by simply improving the accuracy of measurements.

Complementing magnetic measurements with the internal line polarization signal MSE-LP from the motional Stark effect diagnostic, which gives a local information on the ratio B_z/B_φ, makes the σ-curves

less steep and significantly extends the spectrum of "visible" perturbations.

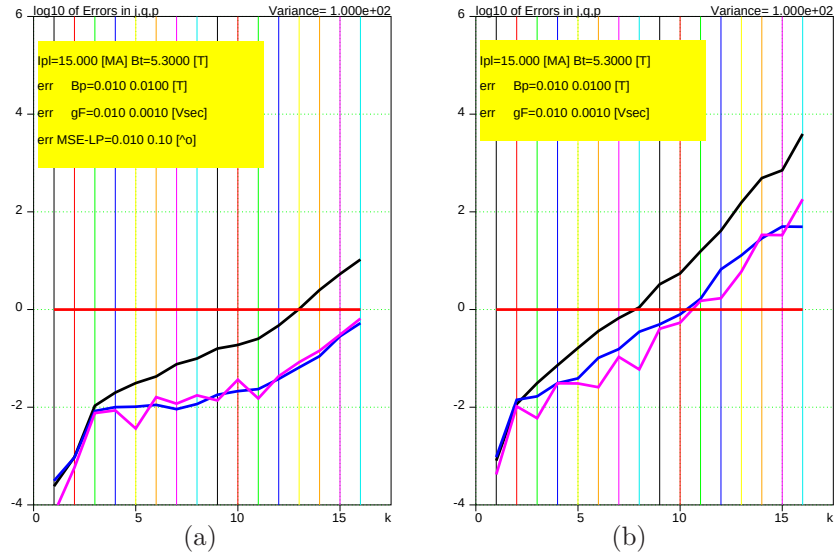

Figure 21: *$\sigma-$ curves* $\log_{10}\{\bar{\sigma}^k, \bar{\sigma}^k_q, \bar{\sigma}^k_p\}$ *for* $\xi = 0$ *and diagnostic system with (a)* Φ*,* B*, and 21 MSE-LP signals, and (b) magnetic signals only* Φ*,* B *(Fig. 16a).*

The σ-curves in Fig. 21 show that the use of MSE-LP reduces the largest RMS values of $\bar{\sigma}^k$, makes 12 perturbations visible, and dramatically improves reconstruction of q- and p-profiles, as in shown in Fig. 22

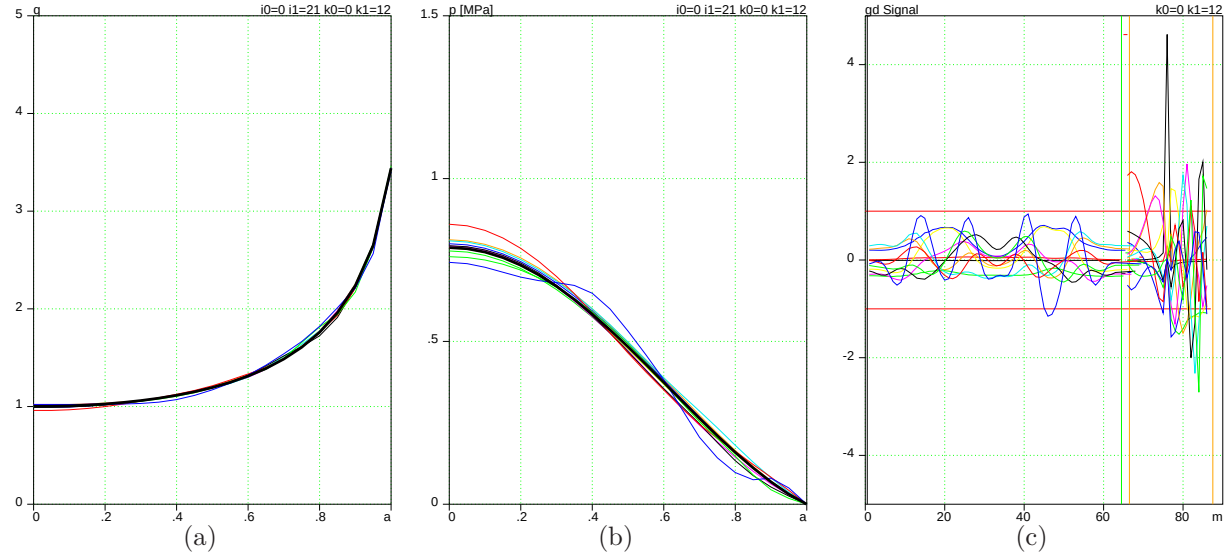

Figure 22: *Variances in (a) q-, and (b) p-profiles as functions of a in the range* $k_J \leq 6$*,* $k_P \leq 6$*. (c) Normalized signals* $\delta\bar{S}_m = \delta S_m/\epsilon_m$ *generated by the eigen-perturbations on the* B*-coils (*$0 \leq m < 64$*),* Φ*-loop (*$m = 64$*) and on MSE-LP (*$65 \leq m < 85$*) diagnostics.*

Fig. 23, which presents the variances for the full spectrum, shows that only perturbations with $k \geq 14$ might be potentially troublesome.

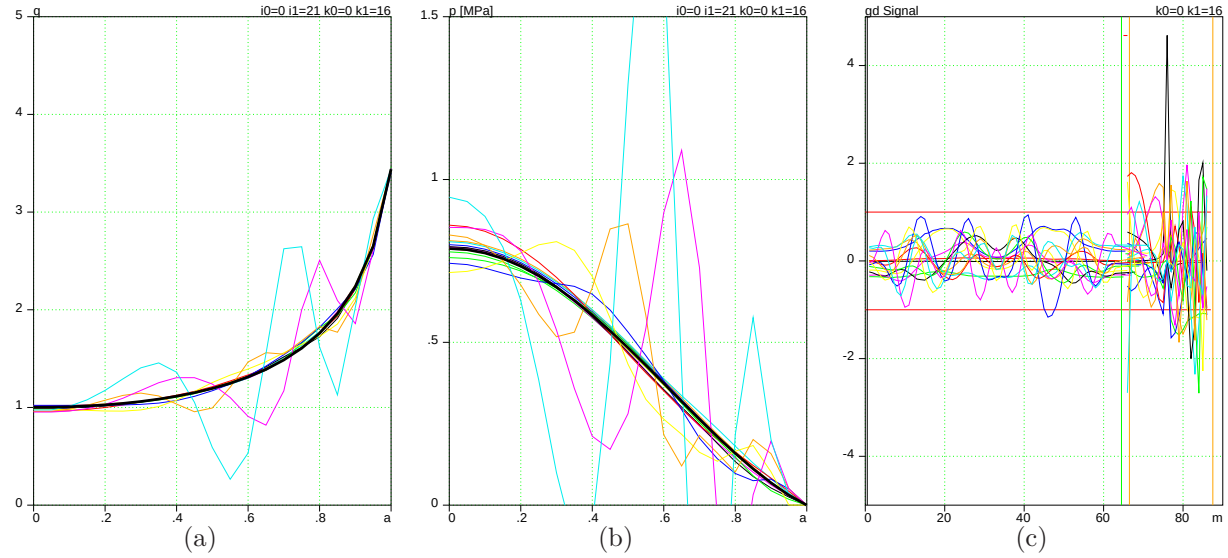

(a) (b) (c)

Figure 23: *Same as in Fig. 22, but for* $k_J \leq 8$, $k_P \leq 8$.

5.3 Evaluation of MSE-LS signals for equilibrium reconstruction *(to ToC)*

Another signal made possible by the motion Stark effect diagnostic, corresponding to the line shift of the Stark spectrum, MSE-LS, can potentially substitute the conventional line polarization signal MSE-LP. The σ-curves for magnetic measurements complemented by MSE-LS exhibits a similar improvement of accuracy of reconstruction as the MSE-LP diagnostics, as is shown in Fig. 24.

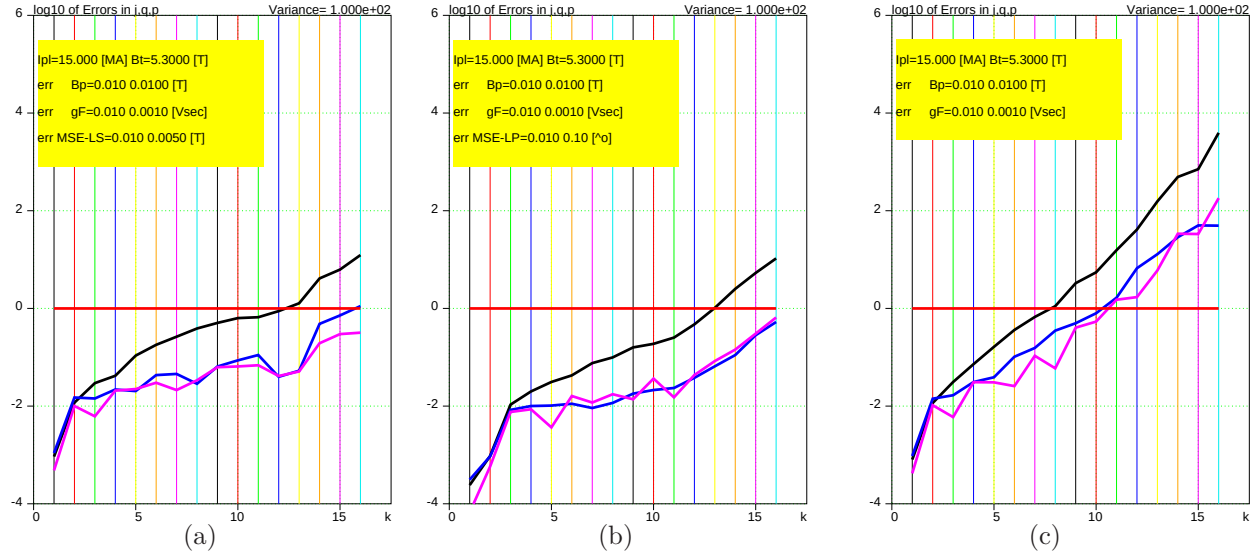

(a) (b) (c)

Figure 24: *σ-curves* $\log_{10}\{\bar{\sigma}^k,\ \bar{\sigma}_q^k,\ \bar{\sigma}_p^k\}$ *for the fixed boundary plasma* $\xi = 0$ *in for a diagnostic system using (a)* Φ *&* B *& MSE-LS signals, (b)* Φ *&* B *& MSE-LP (Fig. 21a), and (c) only magnetic* Φ *&* B *signals (Fig. 16a).*

Variances in reconstructed q and p-profiles using Φ & B & MSE-LS signals (still for a fixed plasma boundary) are given in Fig. 25. Perturbations with $k \leq$12 can be reconstructed using this set of signals.

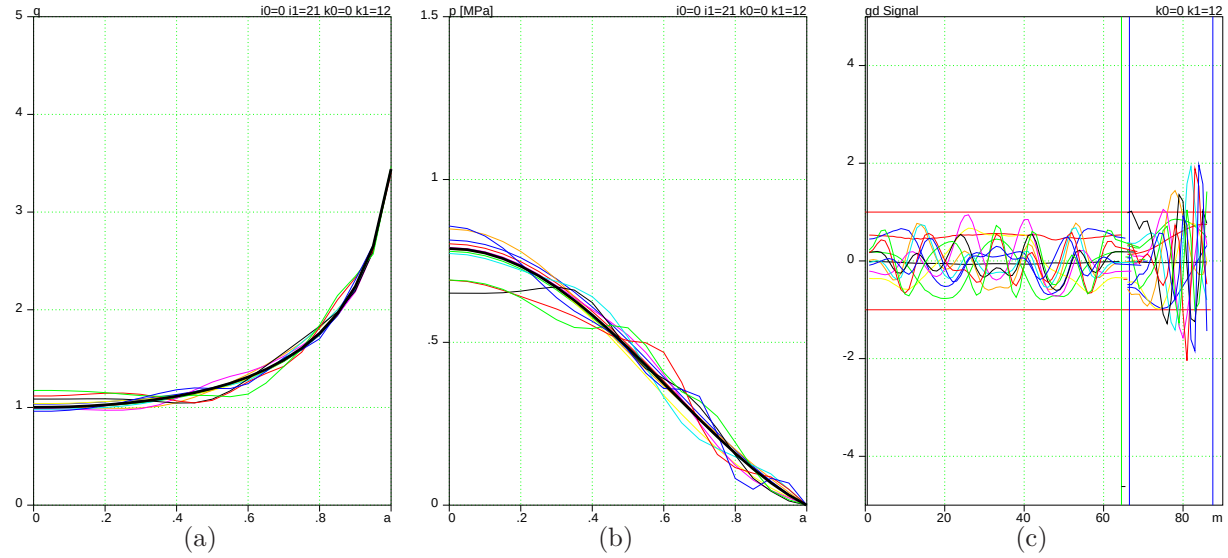

Figure 25: *Variances in (a) q- and (b) p-profiles as functions of a in the range* $k_J \leq 6$, $k_P \leq 6$. *(c) Normalized signals* $\delta\bar{S}_m = \delta S_m/\epsilon_m$ *generated by the eigen-perturbations on the B-coils* ($0 \leq m < 64$)*,* Φ*-loop* ($m = 64$) *and on MSE-LS* ($65 \leq m < 85$) *diagnostics.*

Fig. 26 indicates that only the perturbations with $k > 12$ might be potentially troublesome.

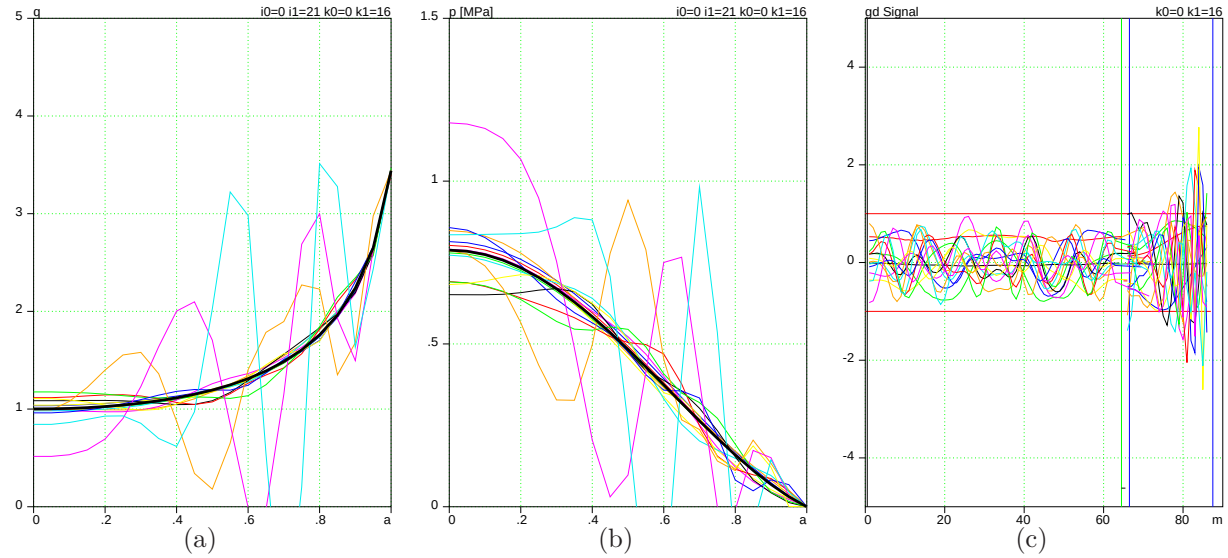

Figure 26: *Same as Fig. 25, but for full spectrum* $k_J \leq 8$, $k_P \leq 8$

Figure 27 demonstrates the effect of improving the relative accuracy of MSE-LS signals by a factor of 10 to the level $\epsilon^{realtive}_{MSE-LS} = 0.1\%$, which may be achievable. This significantly reduces the amplitude of variances in the reconstruction of the q and pressure profile.

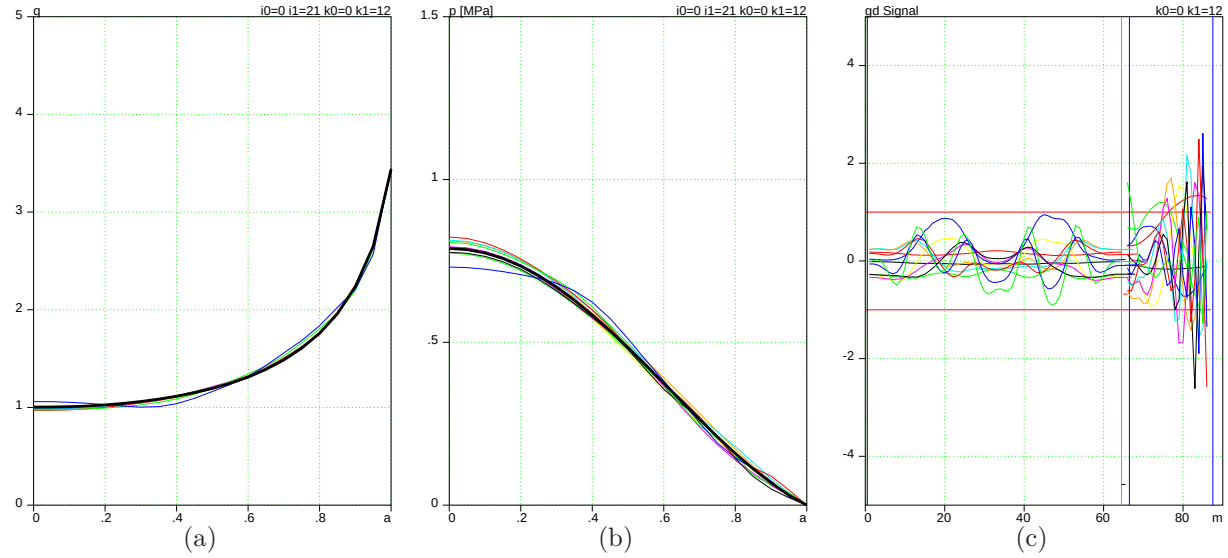

Figure 27: *Same as Fig. 25 ($k_J \leq 6$, $k_P \leq 6$), but with enhanced relative accuracy $\epsilon^{relative}_{MSE-LS} = 0.1\%$.*

The ability of the diagnostic systems with internal measurements to reconstruct the q- and p-profiles is not limited to equilibria with smooth current density profiles. Fig. 28 shows the variances in reconstruction of an equilibrium with a non-monotonic current density. Use of the MSE-LS signal allows one to pick up the details in q-profiles related to the non-monotonic current density.

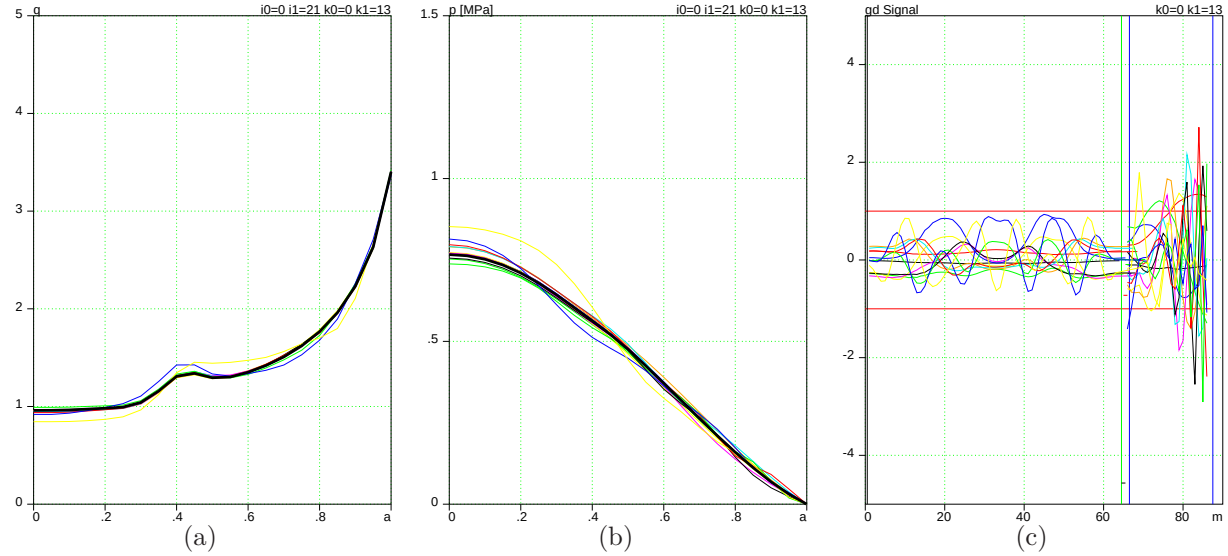

Figure 28: *Same as Fig. 27 ($k_J \leq 6$, $k_P \leq 6$, $\epsilon^{relative}_{MSE-LS} = 0.1\%$) for non-monotonic current density.*

5.4 The possibility of complete reconstruction of the q- and p-profiles *(to ToC)*

The use of both signals MSE-LP and MSE-LS in addition to external magnetic measurements can lead to a possibility of complete reconstruction of q- and p-profiles in a whole spectrum of perturbations, as is indicated in Fig. 29.

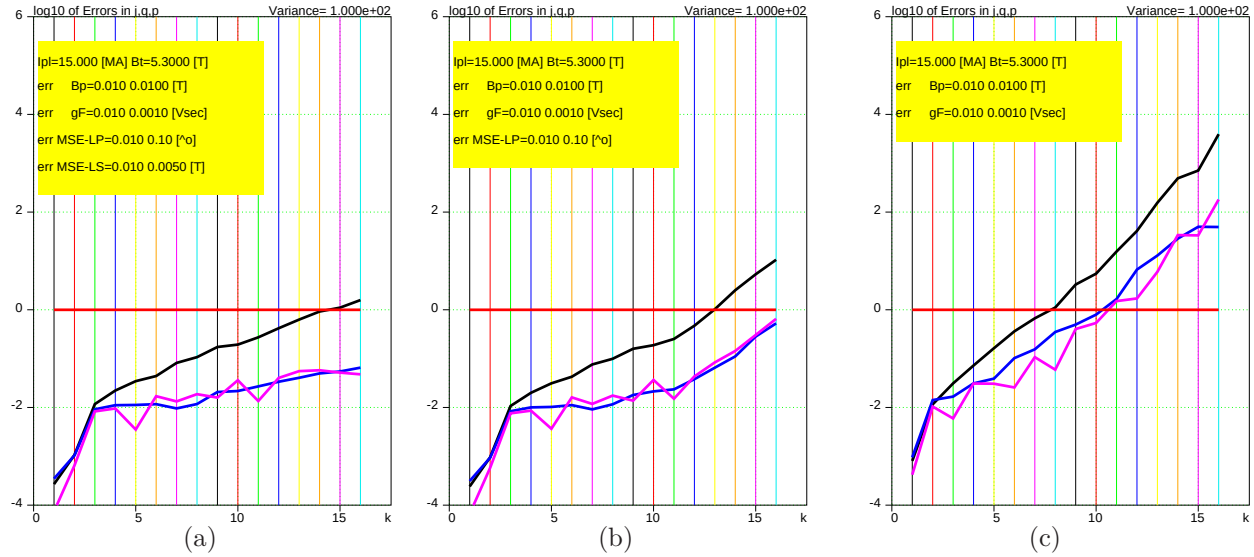

Figure 29: *σ-curves* $\log_{10}\{\bar{\sigma}^k,\ \bar{\sigma}_q^k,\ \bar{\sigma}_p^k\}$ *for diagnostic systems using (a)* Φ *&B & MSE-LP & MSE-LS signals, (b)* Φ *& B & MSE-LP (Fig. 21a), and (c)* Φ *& B only (Fig. 16a).*

In the case of this enhanced set of signals, the σ-curves for variances in q and p have lost their tendency to increase at large k. This behavior of the σ-curves indicates that with an appropriate diagnostic system, the complete reconstruction of q- and p-profiles is possible. On the other hand, the current density still cannot be completely reconstructed.

The variances in q- and p-profiles for the full spectrum of $k \leq 16$ are shown in Fig. 30 for the case of Φ & B & MSE-LP&LS signals.

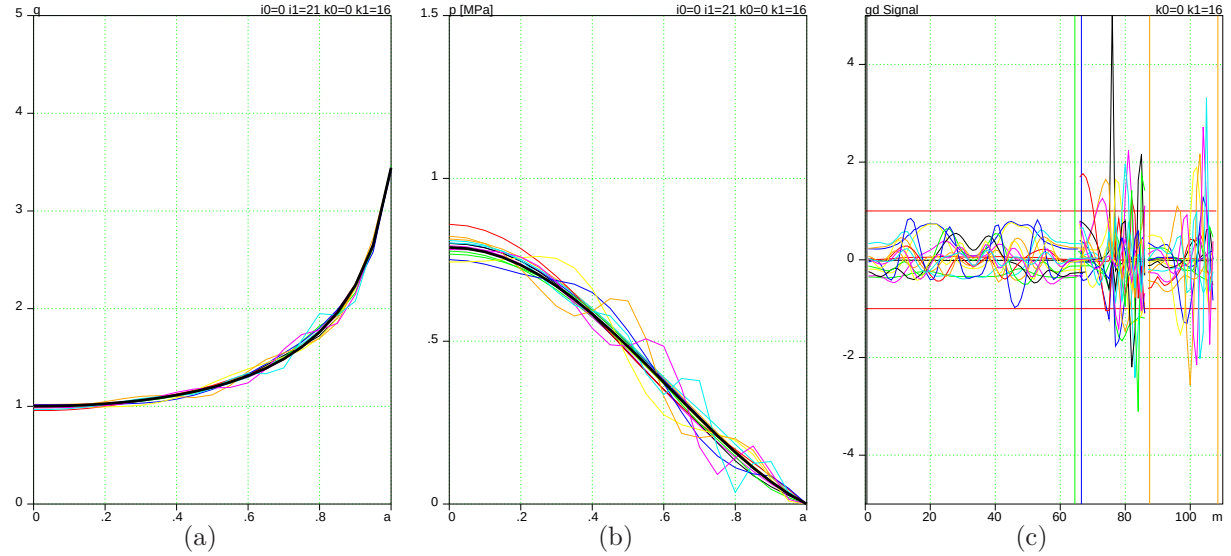

Figure 30: *Variances in (a) q- and (b) p-profiles as functions of a in the full range* $k_J \leq 8$, $k_P \leq 8$. *(c) Normalized signals* $\delta\bar{S}_m = \delta S_m/\epsilon_m$ *generated by the eigen-perturbations on the B-coils (*$0 \leq m < 64$*),* Φ*-loop (*$m = 64$*), on MSE-LP (*$65 \leq m < 85$*), and MSE-LS (*$85 \leq m < 106$*) diagnostics.*

5.5 The effect of free boundary on reconstruction of the q- and p-profiles *(to ToC)*

So far, in all examples it was assumed that the plasma boundary shape was perfectly known. Of course, this in not the case in practice. Nevertheless, because the accuracy of Ψ-flux loop signals is typically good, the uncertainties in the plasma boundary do not affect significantly the overall ability (or inability) of a diagnostic system to reconstruct q- and p-profiles.

The σ-curves, when the plasma boundary and q-, p-profiles were reconstructed using 16 Ψ flux loops in the vicinity of the plasma, together with B-coils, Φ-loop, MSE-LP and MSE-LS signals, are shown in Fig. 31.

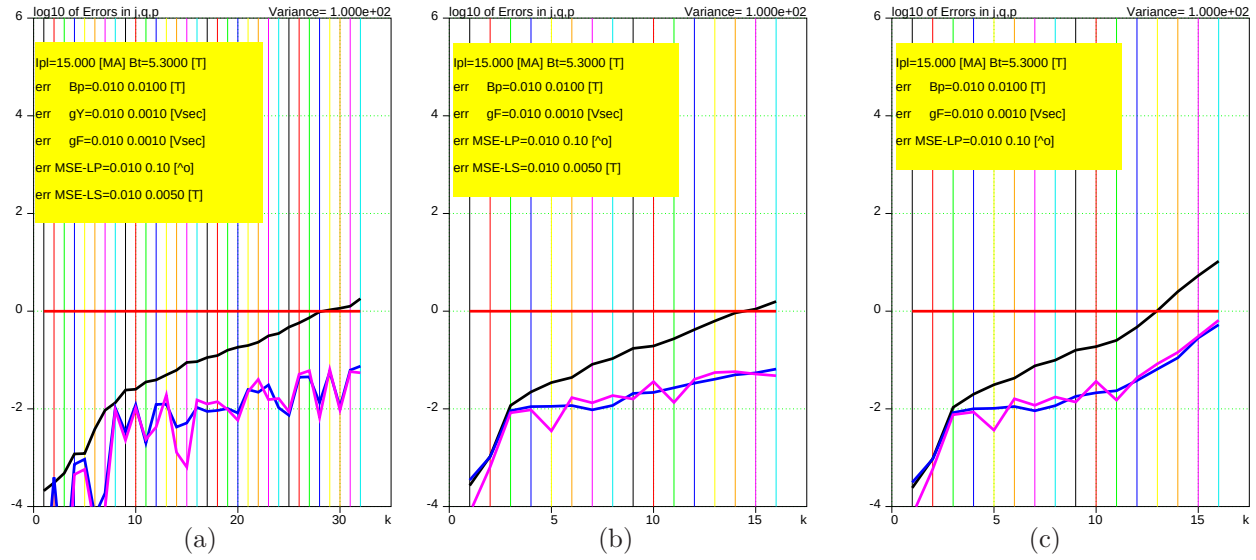

Figure 31: *σ-curves* $\log_{10}\{\bar{\sigma}^k,\ \bar{\sigma}_q^k,\ \bar{\sigma}_p^k\}$ *for free and fixed boundary cases (a) free boundary,* $\xi \neq 0$*, with* Φ *&*B *& MSE-LP & MSE-LS signals, (b) fixed boundary,* $\xi = 0$*, with the same signals (Fig. 29a) (c) fixed boundary,* $\xi = 0$*, with* Φ *&* B *& MSE-LP (Fig. 21a).*

Fig. 32 shows the variances in reconstruction of the q- and p-profiles for a free boundary plasma, which is essentially the same in quality as in the example in Fig. 30. The plot Fig. 32c shows a high role of the Ψ signals in reconstruction.

5.6 Curious case of reconstruction without B-signals *(to ToC)*

It is interesting that the theory of variances predicts, at least hypothetically, a possibility of reconstruction of q- and p-profiles even without B-signals from the local pick up coils. This situation was simulated by a significant reduction in sensitivity of the B-coils.

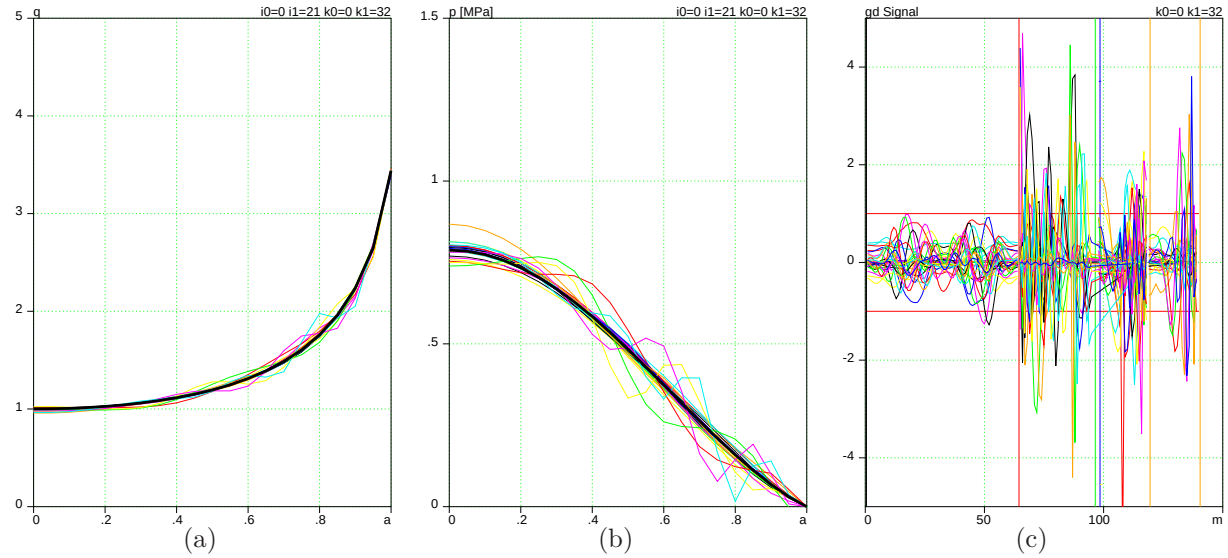

Figure 32: *Variances in (a) q and (b) p-profiles as functions of a in the full range $k_B \le 16$, $k_J \le 8$, $k_P \le 8$. (c) Normalized signals $\delta\bar{S} = \delta S_m/\epsilon_m$ generated by the eigen-perturbations on B-coils ($0 \le m < 64$), Ψ-loops ($64 \le m < 96$), Φ-loop ($m = 96$), in MSE-LP ($97 \le m < 113$) and MSE-LS ($113 \le m < 139$) diagnostics.*

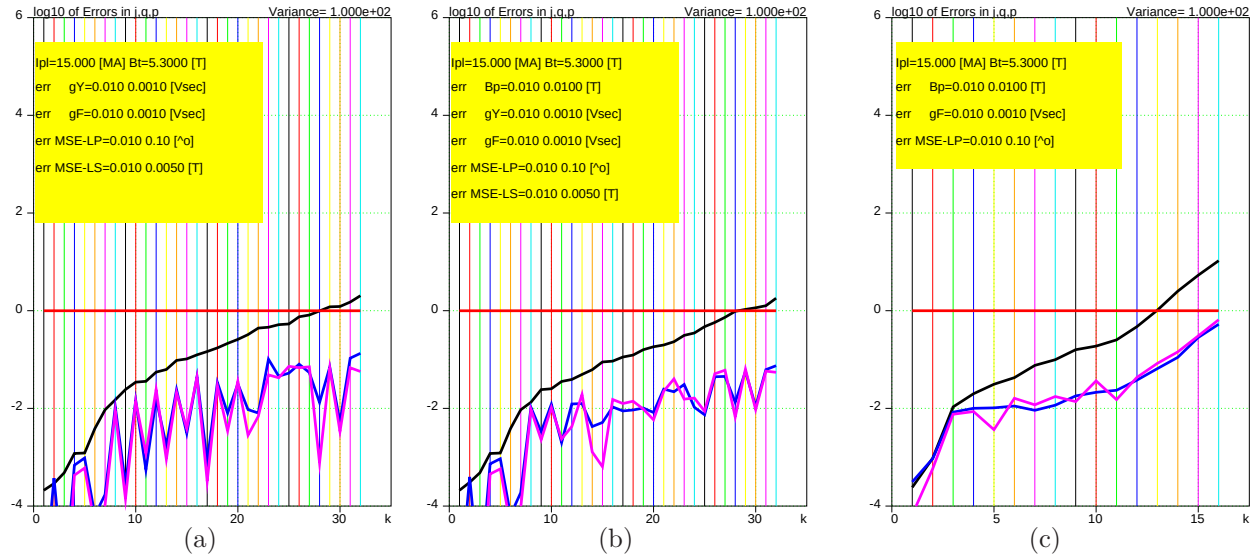

Figure 33: *σ-curves* $\log_{10}\{\bar{\sigma}^k,\ \bar{\sigma}_q^k,\ \bar{\sigma}_p^k\}$ *for free and fixed boundary cases (a) free boundary, $\xi \ne 0$, with Φ & MSE-LP & MSE-LS signals only, (b) free boundary, $\xi \ne 0$, with Φ &B & MSE-LP & MSE-LS signals (Fig. 31a), (c) fixed boundary, $\xi = 0$, with Φ & B & MSE-LP signals (Fig. 21a).*

Fig. 33 show the σ-curves for the case than the Ψ-loops are located in the very vicinity of the plasma boundary (so B-signal are not necessary for reconstruction of the plasma boundary) and Φ-loop, MSE-LP, and MSE-LS are used for reconstruction. The σ_q, σ_p-curves indicate that the q- and p-profiles can be well reconstructed even without B-signals as is shown in Fig. 34.

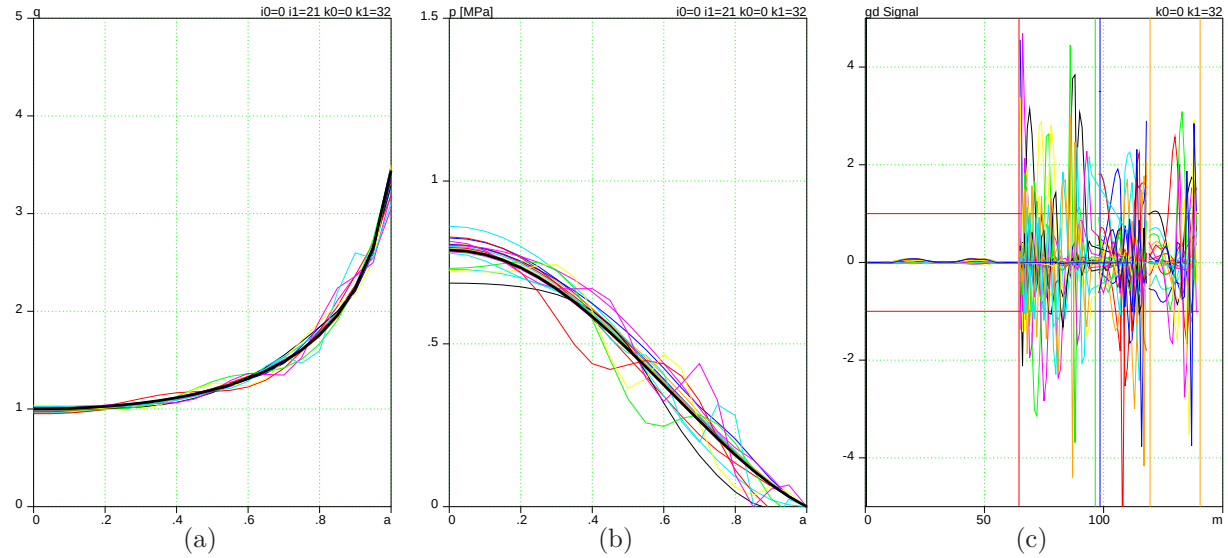

Figure 34: *Same as in Fig. 32, but for the case of very low sensitivity of the B-coils* ($0 \leq m < 64$).

6 Alignment of sensitivities of sensors *(to ToC)*

The technique of analyzing the equilibrium reconstruction allows the use of signals of different physical nature in the process of reconstruction. The normalization of the working matrix using the sensitivity value of every signal takes into account the contributions of every signal in a way that is appropriately independent of the nature of the signal. The same technique provides the assessment of the role of each signal in the reconstruction.

The plots of signals generated by eigen-perturbations in Figs. 17c,18c,19c,20c,22c,23c,25c,26c,27c,28c,30c, 32c,34c show some nonuniformity in the value of different signals relative to the sensitivity of sensors. Correspondingly, the contribution of different signals to the reconstruction is not uniform.

The recipe for the optimal use of diagnostics of different physicale nature is to align the sensitivity of sensors in such a way that the signals $\delta\bar{S}^k_m$ from eigen-perturbations fill up the band $|\delta\bar{S}^k_m| \leq 1$ uniformly. The implementation of this recipe requires a statistical analysis of characteristic cases of reconstruction. We leave this issue for future publications.

7 Use of σ-curves for optimal reconstruction *(to ToC)*

Besides assessment of final reconstruction, the σ-curves can provide information for optimal organization of the iterative solving of the GSh equation in the process of fitting its solution and the current distribution to the measurements.

The problem is in making a compromise between the goal of the most accurate reconstruction and stability of iterations. If the σ-curves were to be calculated at every iteration, then the current distribution could be composed from the eigen-perturbations, whose k-spectrum is limited by the condition of elimination of "invisible" perturbations

$$\log_{10} \bar{\sigma}^k < -r, \tag{7.1}$$

where the constant r is in the range $0.5 < r < 1$. The left boundary here should be determined experimentally from the marginal stability of iterations.

In this way, reconstruction with a poor set of signals, e.g., containing only external measurements, would be performed with a small set of free parameters leading to a reconstruction of limited value. On the other hand, in the case of good diagnostics, the stability of reconstruction will be provided even for the most accurate reconstruction possible.

The practical implementation of this algorithm is left future development.

8 Conclusions *(to ToC)*

The capability of calculating variances, now developed, has essentially completed the theory of equilibrium reconstruction. In particular, the quantitative evaluation of the quality of diagnostic systems on existing and future machines can be done based on spectrum of "visible" perturbations and $\bar{\sigma}$-curves. The theory confirms that internal measurements of the magnetic field are crucial for reconstruction. In this regard, either MSE-LP (line polarization) or MSE-LS (line shift) signals from the plasma in addition to external measurements allow for a complete reconstruction (of both q- and p-profiles). The presented technique can be used to optimize the diagnostic set on any tokamaks. Contribution of any signal can be evaluated. The proposal by Nova Photonics to utilize MSE-LS signals would significantly enhance the equilibrium reconstruction capability in ITER.

Extension of the theory should be focused on realistic simulation of signals used in reconstructions and on developing a working algorithms, based on σ-curves, for accurate and stable iterative solution of the GSh equation for reconstruction purposes.

This work is supported by US DoE contract No. DE–AC020–76–CHO–3073.

References

[1] Shafranov, V. D. Sov. Phys. JETP **6**, 545 (1958); Zh. Eksp. Teor. Fiz. **33**, 710 (1957). H. Grad and H. Rubin, in *Proceedings of the Second United Nations Conference on the Peaceful Uses of Atomic Energy* (UN, Geneva, 1958). Vol.21, p.190.

[2] A. V. Bortnikov, Yu. T. Baiborodov, N. N. Brevnov, L. E. Zakharov, V. G. Zhukovskii, D. V. Orlinskii, V. I. Pergament, M. K. Romanovskii, N. I. Sokolov, Yu. M. Us, *Proceedings of Contributed Papers, Sixth European Conference on Plasma Physics and Controlled Fusion, Moscow, 1973* (European Physical Society, Plasma Physics Division, published by Joint Institute for Nuclear Research) **2**, 349 (1973).

[3] L.L.Lao, H.St.John, R.D.Stambaugh, A.G.Kellman and W.Pfeiffer, 1985 Nucl. Fusion **25** 1611 (1985).

[4] L.L. Lao, J.R.Ferron, R.J.Groebner, W.Howl, H.St.John, E.J.Strait and T.S. Taylor, Nucl. Fusion **30**, 1035 (1990)

[5] L. E. Zakharov and V. D. Shafranov. *Reviews of Plasma Physics* (Consulant Bureau, New York, 1986), Vol.11, p.153.

[6] C. M. Bishop, J. B. Taylor, Proceedings of Contributed Papers, 12th European Conference on Controlled Fusion and Plasma Physics, Budapest, 1985, edited by L. Pócs and A. Montvai (European Physical Society, Budapest, 1985) Vol. II pp. 401-404

[7] Bishop, C. M. and J. B. Taylor. Physics of Fluids **29**, 1444 (1986).

[8] "The polarization of an e.m. wave propagating in a plasma with magnetic shear. The measurement of poloidal magnetic field in a Tokamak" F D Marco and S E Segre Plasma Phys. **14**, 245 (1972)

[9] "Current distribution measurement in a tokamak by FIR polarimetry (invited)" H. Soltwisch Rev. Sci. Instruments **57**, 1939 (1986)

[10] "Measurement of the rotational transform at the axis of a tokamak" W. P. West, D. M. Thomas, J. S. deGrassie, and S. B. Zheng Phys.Rev.Lett. **58**, 2758 (1987)

[11] "Temporal behavior of the plasma current distribution in the ASDEX tokamak during lower-hybrid current drive" K. McCormick, F. X. Sldner, D. Eckhartt, F. Leuterer, H. Murmann, H. Derfler, A. Eberhagen, O. Gehre, J. Gernhardt, G. v. Gierke, O. Gruber, M. Keilhacker, O. Klber, K. Lackner, D. Meisel, V. Mertens, H. Rhr, K.-H. Schmitter, K.-H. Steuer, and F. Wagner Phys.Rev.Lett. **58**, 491 (1987)

[12] "Determination of the Poloidal Magnetic Field Profiles in a Tokamak by Polarization Spectroscopy of an Impurity Ion Line" D.Wrblewski, L.K.Huang, H.W.Moos, and P.E.Phillips, Phys.Rev.Lett. **61**, 1724 (1988)

[13] F.M.Levinton, R.J.Fonck, G.M.Gammel, R.Kaita, H.W.Kugel, E.T.Powell, and D.W.Roberts, Phys.Rev.Lett. **63**, 2060 (1989).

[14] L. E. Zakharov and A. Pletzer, Phys. of Plasmas, v.**6**, p. 4693 (1999)

[15] H. Y. Yuh, E. L. Foley, F. M. Levinton, USIPO Report S006930-F (2007).

[16] W. H. Press, S. A. Teukolsky, W. T. Vetterling, B. P. Flannery, "Numerical Recipes in C", Cambridge University Press, Cambridge, New York, Port Chester, Melbourn, Sydney p. 59-70 (1992)

The Princeton Plasma Physics Laboratory is operated
by Princeton University under contract
with the U.S. Department of Energy.

Information Services
Princeton Plasma Physics Laboratory
P.O. Box 451
Princeton, NJ 08543

Phone: 609-243-2750
Fax: 609-243-2751
e-mail: pppl_info@pppl.gov
Internet Address: http://www.pppl.gov